Chinese Journal of Natural Medicines

Naringenin ameliorates iron overload–associated osteoporosis *via* Tfeb/p62/Nrf2–mediated antioxidation

Zhaofeng Pan, Miao Li, Baihao Chen, Jiaxin Lu, Fanchen Wang, Chenhui Meng, Xintian Wang, Min Shao, Qi He, Haibin Wang

Citation: Zhaofeng Pan, Miao Li, Baihao Chen, Jiaxin Lu, Fanchen Wang, Chenhui Meng, Xintian Wang, Min Shao, Qi He, Haibin Wang, Naringenin ameliorates iron overload–associated osteoporosis *via* Tfeb/p62/Nrf2–mediated antioxidation, Chinese Journal of Natural Medicines, 2026, 24(8), 912–928. doi: 10.1016/S1875–5364(26)61193–4.

View online: https://doi.org/10.1016/S1875–5364(26)61193–4

Related articles that may interest you

Luteoloside protects the vascular endothelium against iron overload injury *via* the ROS/ADMA/DDAH Ⅱ/eNOS/NO pathway

Chinese Journal of Natural Medicines. 2022, 20(1), 22–32 https://doi.org/10.1016/S1875–5364(21)60110–3

Activation of NRF2 by celastrol increases antioxidant functions and prevents the progression of osteoarthritis in mice

Chinese Journal of Natural Medicines. 2024, 22(2), 137–145 https://doi.org/10.1016/S1875–5364(24)60586–8

Effects of chitooligosaccharide–zinc on the ovarian function of mice with premature ovarian failure *via* the SESN2/NRF2 signaling pathway

Chinese Journal of Natural Medicines. 2021, 19(10), 721–731 https://doi.org/10.1016/S1875–5364(21)60084–5

Ethanol extract of Cyathulae Radix inhibits osteoclast differentiation and bone loss

Chinese Journal of Natural Medicines. 2024, 22(3), 212–223 https://doi.org/10.1016/S1875–5364(24)60596–0

Targeting TLR4 and regulating the Keap1/Nrf2 pathway with andrographolide to suppress inflammation and ferroptosis in LPS–induced acute lung injury

Chinese Journal of Natural Medicines. 2024, 22(10), 914–928 https://doi.org/10.1016/S1875–5364(24)60727–2

Loganin inhibits the ROS–NLRP3–IL–1β axis by activating the NRF2/HO–1 pathway against osteoarthritis

Chinese Journal of Natural Medicines. 2024, 22(11), 977–990 https://doi.org/10.1016/S1875–5364(24)60555–8

Wechat

Chinese Journal of Natural Medicines 24 (2026) 912-928

Contents lists available at ScienceDirect

Chinese Journal of Natural Medicines

journal homepage: www.cjnmcpu.com/



Original article

Naringenin ameliorates iron overload-associated osteoporosis *via* Tfeb/p62/Nrf2-mediated antioxidation

Zhaofeng Pan[a, e, g, Δ], Miao Li[b, d, g, Δ], Baihao Chen[b, d, f, g, Δ], Jiaxin Lu[a, e], Fanchen Wang[b, d], Chenhui Meng[b, d, g], Xintian Wang[b, d, g], Min Shao[h, *], Qi He[b, d], Haibin Wang[b, c, d, g, *]

[a] *The Third School of Clinical Medicine, Guangzhou University of Chinese Medicine, Guangzhou 510405, China*
[b] *The First School of Clinical Medicine, Guangzhou University of Chinese Medicine, Guangzhou 510405, China*
[c] *The Laboratory of Orthopaedics and Traumatology of Lingnan Medical Research Center, Guangzhou University of Chinese Medicine, Guangzhou 510405, China*
[d] *Department of Orthopaedic Surgery, The First Affiliated Hospital, Guangzhou University of Chinese Medicine, Guangzhou, Guangdong 510405, China*
[e] *The Third Affiliated Hospital of Guangzhou University of Chinese Medicine, Guangzhou 510378, China*
[f] *The Fifth School of Clinical Medicine, Guangzhou University of Chinese Medicine, Guangzhou 510405, China*
[g] *State Key Laboratory of Traditional Chinese Medicine Syndrome, The Second Affiliated Hospital of Guangzhou University of Chinese Medicine, Guangzhou 510120, China*
[h] *Guangzhou University of Chinese Medicine, Guangzhou 510405, China*

ARTICLE INFO

Article history:
Received 10 October 2025
Revised 15 December 2025
Accepted 6 February 2026
Available online 20 August 2026

Keywords:
Iron overload
Naringenin
Osteoporosis
Tfeb/p62/Nrf2 Pathway
Bone formation

ABSTRACT

Postmenopausal women, elderly individuals, and transfusion-dependent patients are prone to bone marrow iron overload, which is closely associated with iron overload-associated osteoporosis (IOOP). Currently, the treatment of IOOP mainly focuses on promoting iron efflux and alleviating iron-induced damage, but the intervention value of natural active ingredients remains unclear. Naringenin (NAR), as a natural flavonoid, can regulate bone metabolism, yet its role and mechanism in IOOP have not been elucidated. In this study, an *in vitro* model was established by inducing MC3T3-E1 cells with ferric ammonium citrate (FAC), and an *in vivo* IOOP model was constructed by inducing mice with iron dextran to investigate the effects and mechanisms of NAR. The results showed that NAR improved the alkaline phosphatase (ALP) activity and mineralization capacity of FAC-induced iron-overloaded cells, upregulated the expression of collagen I (Col1a1) and runt-related transcription factor 2 (Runx2), reduced the accumulation of reactive oxygen species (ROS) and lipid peroxide (LPO), attenuated mitochondrial membrane potential (MMP) impairment, and inhibited apoptosis. In *in vivo* experiments, NAR restored the density and quantity of trabecular bone in iron-overloaded mice. Mechanistically, RNA sequencing indicated that the effect of NAR was associated with transcription factor EB (Tfeb)-dependent transcription: NAR promoted Tfeb nuclear translocation and upregulated p62 transcription under iron overload conditions. Co-immunoprecipitation (Co-IP) demonstrated that NAR enhanced the binding of p62 to kelch-like ECH associated protein 1 (Keap1), while increasing Nrf2 phosphorylation and upregulating its key effector proteins HO-1 and NQO1. Functional validation showed that the Nrf2 antagonist ML385 or siRNA could block the effects of NAR without affecting Tfeb expression, whereas the Tfeb inhibitor eltrombopag simultaneously inhibited Nrf2 expression and NAR-induced effects. In conclusion, NAR alleviates iron overload-induced oxidative damage and osteogenic disorders *via* the Tfeb/p62/Nrf2 pathway, suggesting that it may serve as a potential therapeutic agent for IOOP.

1. Introduction

Osteoporosis (OP) is a prevalent orthopaedic disease on a global scale [1, 2], the aetiology of which is multifactorial [3]. It is characterised by a decrease in bone density and quality due to the destruction of the microstructure of the bone, thereby increasing bone fragility [1].

The stability of the skeletal structure is contingent upon the metabolic balance of bone, a process that is subject to rigorous regulation by a complex series of mechanisms [4]. Osteoblasts, derived from the mesenchymal cells of the pluripotent bone marrow stroma, form bone nodules by synthesising and secreting matrix proteins such as Col1a1 and osteocalcin for eventual mineralisation [5]. Following matrix mineralization, approximately 60%–80% of osteoblasts undergo apoptosis, whereas the surviving cells differentiate into osteocytes and bone lining cells [6]. Maintaining the right balance between bone matrix formation by osteoblasts and bone resorption by osteoclasts is essential for bone homeostasis [6-8].

* Corresponding author.
E-mail addresses: shaomin98@aliyun.com (M. Shao); wanghaibin0058@gzucm.edu.cn (H. Wang)
Δ These authors contributed equally to this work.

https://doi.org/10.1016/S1875-5364(26)61193-4
Copyright © 2026, China Pharmaceutical University. Published by Elsevier B.V. All rights are reserved.

Iron, as an essential trace element crucial for human physiological processes, plays a pivotal role in maintaining bone homeostasis [9, 10]. Inspired by recent studies [11-15], the link between iron and osteoporosis has recently received increased attention. Iron can be obtained daily from food and is essential in many biochemical processes such as oxygen transport, bone marrow haematopoiesis and immune responses [12]. Various physiological and pathological processes, such as tumours [16], atherosclerosis [17] and osteoporosis [12, 18] have been linked to iron overload.

IOOP originates from disrupted iron homeostasis, leading to compromised bone integrity, reduced bone mass, and microarchitectural deterioration [18]. Under physiological conditions, iron equilibrium is tightly regulated through ferritin-mediated buffering [19]. However, in specific pathological contexts—including postmenopausal women, elderly populations, chronic transfusion-dependent patients, and hereditary hemochromatosis—bone marrow iron overload induces oxidative damage *via* Fenton/Haber-Weiss reactions that generate excessive ROS [20]. While physiological ROS levels are essential for cellular signaling, pathological ROS accumulation causes DNA damage and mitochondrial dysfunction [21], contributing to skeletal pathologies such as osteopetrosis. Osteogenesis requires coordinated mitochondrial energy production to support cellular reprogramming. Although the precise mechanisms remain incompletely defined, iron overload-associated ROS attack DNA and mitochondria, promoting osteoblast apoptosis [22], cellular senescence [23], iron death [24], and impaired osteoblast proliferation/mineralization [25]. The iron chelator deferoxamine (DFO) has demonstrated efficacy in alleviating postmenopausal osteoporosis by modulating skeletal iron dynamics [13]. Nevertheless, the molecular pathways linking iron overload to impaired bone formation require further investigation.

The Tfeb/Nrf2 system is the core regulatory network for cells to respond to oxidative stress, and its molecular composition and function are highly synergistic. Nrf2 (nuclear factor E2-related factor 2) belongs to the CNC-bZIP transcription factor family, which binds to Keap1 through the Neh domain and is ubiquitinated and degraded in the basal state [26, 27]; while oxidative stress or electrophilic stimulation can destroy the Keap1-Nrf2 complex, prompting Nrf2 to enter the nucleus and bind to the ARE [28], activating HO-1, GSTM1 and other antioxidant genes [29].

As a member of the MiT/TFE family, Tfeb and Nrf2 have a significant intersection in the regulatory network: the Keap1-Nrf2 pathway enhances the cell's ability to clear oxidative damage products by upregulating TFEB/TFE3-dependent lysosome biogenesis [30]; at the same time, Tfeb inhibits the E3 ubiquitin ligase DCAF11 of Nrf2 and promotes the phosphorylation of p62, blocking the degradation of Nrf2 mediated by Keap1 [31], forming a positive feedback loop to amplify the antioxidant signal [32]. This regulatory synergy makes the Tfeb/Nrf2 system a key hub for maintaining oxidative-reduction homeostasis.

Plant-derived bioactive extracts are one of the key sources of natural medicines [33, 34]. NAR is a flavonoid compound that is found in a wide variety of plants, with a particular prevalence in citrus fruits. It is not only one of the important active ingredients of traditional Chinese medicines, such as Drynariae Rhizoma (GuSuiBu) and Citri Grandis Exocarpium (HuaJvHong) [35]. NAR has been shown to have a range of biological effects. Similar to most botanical drugs [36], it also possesses anti-inflammatory [37], antioxidant [38], immunomodulatory [39], and anti-tumor [40]. In previous studies, NAR has been found to enhance the antioxidant capacity of cells, which is crucial in combating oxidative stress. Furthermore, NAR has been reported in the treatment of various animal models of osteoporosis [41, 42]. However, the role of NAR in IOOP remains to be elucidated, and its specific mechanisms are yet to be fully understood.

2. Materials and methods

2.1. Materials and reagents

Detailed information for reagents and equipment is listed in Supplementary Tables S1 and S2.

2.2. Animal experiments

C57BL/6J mice (males, six weeks old, 20 ± 3 g) used in this study were purchased by the Experimental Animal Center of Guangzhou University of Chinese Medicine [SCXK (YUE) 2018-0034]. After one week of acclimatisation feeding, the animals were randomly divided into five groups of 8 mice each: Control group (weekly 0.9% sodium chloride injections intraperitoneally at 8 to 18 weeks old, daily gavage with distilled water from 12 to 18 weeks old), FeDx group (weekly 0.5 g·kg^{-1} iron dextran injections intraperitoneally at 8 to 18 weeks old, this intervention was used in the remaining groups except the control group) [23], FeDx + NAR-L group (60 mg·kg^{-1} NAR was administered by gavage daily from 12 to 18 weeks old), FeDx + NAR-H group (120 mg·kg^{-1} NAR was administered by gavage daily from 12 to 18 weeks old) [43]. The positive control group received DFO 250 mg·kg^{-1} (saline) intervention in addition to the administration of FeDx [14]. All animals were housed in experimental animal facilities (Laboratory Animal Centre, The First Affiliated Hospital of Guangzhou University of Chinese Medicine, SYXK 2018–0092). The corncob granules are changed every 2 days, food and drinking water are replenished, and the environment is ventilated and tidy. The light source was switched on and off alternately for 12 h to simulate day and night cycles, and the mice were allowed to eat freely inside the cages. Rearing ended at 18 weeks of age, and after euthanasia by CO_2, lower limb bone samples were collected and processed for further processing. This animal experiment (Fig. 1A) was approved by the Animal Ethics Committee of the First Affiliated Hospital of Guangzhou University of Chinese Medicine (Approval No. 2021029).

2.3. Cell culture

Reference to previous literature [44], MC3T3-E1 cells were purchased from Wuhan Punosai Biological Company (China) and maintained in minimal essential medium (α-MEM, servicebio, G4554, China) at 37 °C containing 5% CO_2 supplemented with 1% penicillin-streptomycin (Gibco, 15070063, USA) and 10% fetal bovine serum(Gibco, 10099-141, USA).

2.4. CCK-8 assay

To screen for effective initial concentrations of NAR, MC3T3-E1 cells (4 × 10^3 cells/well) were inoculated in 96-well cell culture plates and then exposed to different concentrations of NAR (0, 5, 10, 20, 40, and 80 μmol·L^{-1}) [45] or FAC (0, 25, 50, 100, 200 and 400 μmol·L^{-1}) for various periods (24, 48 or 72 h) [22, 46, 47]. Afterwards, we measured cell viability using CCK-8 (GLPBIO, GK10001, USA). The absorbance was measured at 450 nm using a microplate reader (Multiskan SkyHigh, Thermo Scientific, USA). After that, cells were intervened using a reasonable NAR with FAC (24, 48, or 72 h) to estimate the optimal therapeutic concentration range of the NAR.

2.5. Co-inmunoprecipitation (Co-IP)

Cells were lysed at the end of the culture using a protease inhibitor-containing lysis solution. Samples for Co-IP were incubated overnight at 4 °C with 5 μg of antibody. The lysate-antibody

mixture was centrifuged at 20 000 × *g* for 10 min, and the supernatant was incubated with protein A/G agarose (Thermo Scientific, 20421, USA) at 4 °C for 2 h. The microspheres containing the immunoprecipitated protein complexes were washed four times with IP lysis buffer and denatured for 5 min at 95 °C by adding 2 × SDS-protein loading buffer and subsequently used for gel protein electrophoresis.

2.6. Western blot

The cells are lysed in RIPA lysis solution containing protease inhibitors, and the tissue/cell lysates are centrifuged at 21 000 × *g* for 20 min to remove cell debris. Alternatively, nuclear proteins can be extracted using the nuclear protein extraction reagent. Equal amounts of protein samples (80–100 μg) were prepared and mixed with loading buffer, then subjected to SDS-PAGE using 15% or 10% acrylamide gels and transferred to nitrocellulose membranes. Membranes were blocked with 5% BSA for 1 h at room temperature, then overnight in 5% BSA at a 1∶1000 dilution with the indicated primary antibodies, followed by appropriate HRP-coupled anti-mouse/rabbit secondary antibodies. PVDF membranes containing the target proteins were immersed using ECL chemiluminescent substrate (ultra sensitive), and then protein band pictures were obtained using a Bio-Rad gel imaging system.

2.7. ALP activity assay and ARS staining

MC3T3-E1 cells were seeded in 24-well plates at a density of 5×10^4 cells per well. After overnight routine culture, the medium was replaced with osteogenic induction medium, and the corresponding pharmacological treatments were applied concurrently. Post-intervention cells were cultured in osteogenic induction medium for 5 d and ALP activity was measured according to the BCIP/NBT ALP colour development kit. The intervened cells were cultured in osteogenic induction medium for 12 d and cell mineralization was detected using ARS staining solution.

2.8. Immunofluorescence assay

MC3T3-E1 cells were inoculated on confocal culture dishes with a glass bottom diameter of 20 mm and fixed in 4% paraformaldehyde after treatment. After being closed with 4% bovine serum albumin (BSA) and washed with PBS, cells were treated with Nrf2 (1∶200, AB_2833793; Affinity Biosciences, USA), Keap1 (1∶150, sc-514914; Santa Cruz Biotechnology, USA) antibodies overnight at 4 °C. Cells were then incubated with Alexa Fluor® 488-labelled goat anti-mouse IgG (1∶500, ab150113; Abcam, UK) or Alexa Fluor® 647-labelled goat anti-rabbit IgG (1∶500, ab150079; Abcam, UK) for 1 h at 25 °C. Cells were re-stained with a DAPI staining solution (Biosharp Biotechnology, China), and fluorescence was detected using a confocal microscope (Leica, Germany).

2.9. Evaluation of intracellular and LPO levels

ROS levels were measured using the DCFH-DA probe-based ROS assay kit. Cells were combined with 20 μmol·L^{-1} DCFH-DA and incubated for 30 min at 37 °C under light-proof conditions. Cells were washed twice with PBS resuspended and assayed on a fluorescence microscope or flow cytometer. Detection of LPO was performed using the BODIPY® 581/591 C11 probe (Thermo Scientific, D3861, USA). Treated cells were mixed with 10 μmol·L^{-1} BODIPY® 581/591 C11, incubated for 35 min at 37 °C under light-proof conditions, washed twice, and then transferred to a feeding tube for detection by flow cytometry.

2.10. Evaluation of mitochondrial ROS (mtROS) levels

The measurement of mitochondrial superoxide in MC3T3-E1 cells was performed with the MitoSOX Red probe. Cells were plated in 24-well plates at an initial density of 2×10^4 cells per well. Following 24 h of culture to ensure cell attachment, the designated pharmacological interventions were initiated. Upon completion of the treatments, the culture medium was aspirated, and the cell monolayer was gently rinsed twice with pre-warmed PBS. A 2.5 μmol·L^{-1} MitoSOX red working solution, prepared in a suitable buffer, was then added to completely cover the cells. The plates were protected from light and incubated at 37 °C for 10 min. Subsequently, the staining solution was removed, and cells were washed twice thoroughly with PBS to minimize non-specific background fluorescence. Imaging was immediately conducted using a fluorescence microscope configured with appropriate filter sets for the red fluorescence emitted by the oxidized probe.

2.11. Evaluation of malondialdehyde (MDA) levels

The lipid peroxidation product MDA level was measured to assess oxidative stress. Briefly, MC3T3-E1 cells were seeded in 48-well plates at a density of 1×10^4 cells per well and allowed to adhere for 24 h under standard culture conditions. The designated pharmacological interventions were initiated on the following day. After treatment, the cells were collected and lysed. The MDA content in the cell lysates was then quantified using a commercial MDA assay kit, strictly following the manufacturer's instructions. The absorbance of the resulting reaction product was measured at 532 nm using a microplate reader (Multiskan SkyHigh, Thermo Scientific, USA).

2.12. Apoptosis evaluation

Apoptosis was detected using Annexin V-FITC/PI kit according to the instructions for use. Cells were inoculated in 6-well plates at a density of 3×10^5, picked up and treated differently. Cells were then digested using trypsin, transferred to EP tubes, and incubated with 10 μL Annexin V-FITC and 5 μL PI in a dark environment for 5 min at 25 °C. Apoptosis was detected by flow cytometry (BD Biosciences, USA) after the addition of 500 μL of loading buffer. Results were analysed using FlowJo 10.6.2 software.

2.13. Mitochondrial membrane potential measurement

The MMP was detected using the JC-1 MMP detection kit. Cells were treated in the same way as for the apoptosis assay. For fluorescence microscopy, cells were washed twice with PBS at the end of treatment, added to JC-1 working solution and incubated for 25 min at 37 °C under protection from light. After incubation, cells were washed twice with JC-1 staining buffer and observed under fluorescence microscopy. For flow cytometry, cells were digested with trypsin at the end of treatment, transferred to 1.5 mL EP tubes and incubated using the same conditions as for fluorescence microscopy. After incubation, the cells were washed twice with JC-1 staining buffer, resuspended and detected by flow cytometry (BD Biosciences, USA).

2.14. Micro-computed tomography (μCT) analysis

After fixation, the bones were placed in a scanning rack on a Skyscan 1172 (Bruker, Germany) and scanned at 80 kV, 100 μA, 0.4° rotation step, and 0.5 mm aluminium filter and 5 μm slice thickness. The data were then analysed using the Custom Analysis Program (CTAn 1.17.7.2, Bruker, Germany). The volume of interest was the trabecular parameters within a secondary trabecular region 130 μm from the proximal tibial growth plate's proximal edge.

2.15. Histology assay

The femur was fixed in 4% paraformaldehyde for 24 h, removed and washed 2 times with PBS. It was then placed in 14% EDTA for decalcification for 10 day. The EDTA solution was changed every 2 day. After dehydration in gradient ethanol, the tissue was embedded in paraffin and sliced into thin sections of 5 μm thickness using a manual rotary slicer (Leica, Germany). Before staining, sections were deparaffinized, rehydrated, and treated with 3% H_2O_2 in methanol to block endogenous peroxidase. Antigen retrieval was performed with heat in citrate buffer, followed by PBST washing and blocking with 10% goat serum. Sections were incubated with primary antibodies overnight at 4 °C, then with HRP-conjugated secondary antibodies for 1 h. After DAB staining, sections were dehydrated, coverslipped, and observed. Negative controls omitted the primary antibody. The sections were stained with H&E staining solution and scanned using a Panoramic Midi Digital Slide Scanner (3DHISTECH, Hungary). The results were viewed and analysed using SlideViewer 2.7 software (3DHISTECH, Hungary).

2.16. Elisa assay

Blood samples were collected from each group of mice and then centrifuged at 1000 × *g* for 10 min to rapidly and carefully separate serum from erythrocytes and collect the serum supernatant. Serum levels of alanine aminotransferase, nitrogen-based aminotransferase and urea were determined according to Elisa instructions.

2.17. RNA-sequencing and data analysis

We extracted the total RNA from the cancellous bone region of the lower femur in mice treated with FeDx and NAR-H. Sample RNA integrity and potential DNA contamination were analyzed using agarose gel electrophoresis. RNA purity was assessed *via* a nanodrop micro-spectrophotometer by measuring $OD_{260/280}$ and $OD_{260/230}$ ratios. RNA integrity was precisely evaluated using an Agilent 2100 Bioanalyzer. Following quality checks, mRNA was enriched using mRNA Capture Beads, purified *via* magnetic bead processing, and fragmented by high-temperature treatment. The fragmented mRNA served as a template for synthesizing first-strand cDNA in a reverse transcriptase mix. During second-strand cDNA synthesis, end repair and A-tailing were simultaneously performed. Adapters were then ligated, and target fragments were purified and selected using Hieff NGS® DNA Selection Beads. PCR amplification of the library was conducted, followed by sequencing on an Illumina Novaseq X Plus platform. Raw data were analyzed by GENE DENOVO Co., Ltd. (China). Gene expression levels were quantified as fragments per kilobase of transcript per million mapped fragments (FPKM), and $\log_2$ (fold change) > 1 or < −1 was considered statistically significant.

2.18. Nfe2l2 gene knockdown and efficiency verification

MC3T3-E1 cells were seeded into culture plates and allowed to grow for approximately 24 h to reach about 70% confluence at the time of transfection. Three individual *Nfe2l2*-targeting siRNAs and one negative control siRNA were complexed with the transfection reagent in Opti-MEM medium. The mixture was incubated at room temperature for 20 min to allow the formation of transfection complexes. These complexes were then added directly to the cell culture medium. After 4 h of transfection, the medium was replaced with fresh complete medium. Following an appropriate incubation period to allow for gene knockdown, the transfection efficiency was assessed by quantifying the mRNA expression level of *Nfe2l2* using quantitative qRT-PCR and its protein expression level using Western blot analysis. The siRNA demonstrating the highest knockdown efficiency was selected for all subsequent functional validation experiments.

2.19. Statistical analyses

Statistical analyses using SPSS 21.0. All results were expressed as mean ± standard deviation. S-W test was used to test whether the data satisfied normal distribution. Comparisons of data between multiple groups were analysed using ANOVA, and differences between two groups were compared using Tukey's test. Data comparisons between various groups that did not satisfy the chi-square test were analysed using the Brown-Forsyth test to compare overall differences. Then the Tamhane T2 test was used to compare two-by-two differences. Statistical results $P < 0.05$ were considered statistically significant. Graphs were created using GraphPad Prism, version 10.

3. Results

3.1. NAR ameliorates bone microstructural changes in IOOP

In this study, an iron overload-induced osteoporosis model was established by intraperitoneal injection of FeDx in animal experiments. After the experiments, the lower limb bones and serum of the mice were collected for subsequent analyses (Fig. 1A). The pathological results showed that after intraperitoneal injection of iron dextran, the bone microstructure of the mice was altered in a poor direction. Bone trabeculae are the supporting structures within the bone marrow cavity. Under iron overload, the number of trabeculae in the tibial marrow cavity was reduced, their length was shortened, and the divisional gap was widened. A more disorganized distribution of trabeculae could be seen in the simulated light 3D model (Fig. 1B). Compared to the Control group, the overall number of bone trabeculae in the model group is sparser, with more peripheral fine shadows, indicating that the bone trabeculae are farther apart and have a smaller and shorter morphology. On computational analysis of the microstructure, the ratio of bone volume to tissue volume (BV/TV) and trabecular bone number (Tb. N) were all reduced in the FeDx group compared to the control group, while the trabecular separation (Tb. Sp). It should be noted that changes in trabecular bone pattern factor (Tb. Pf) following FeDx administration did not reach statistical significance (Figs. 1C–1F). On H&E-stained sections, a marked increase in fatty vesicles could be seen in the FeDx group compared to the Control group, and the cross-sectional random distribution of trabeculae became looser (Fig. 1B).

After treatment with NAR, BV/TV and Tb. N increased while Tb. Pf and Tb. Sp decreased compared to the FeDx group, 120 $mg \cdot kg^{-1}$ of NAR have a better effect. An increase in the number and density of trabeculae with a more regular alignment direction was also clearly observed in the 3D model. DFO is an iron chelator that has been reported in previous studies as a positive control drug for inhibiting iron overload [14]. In IOOP, the use of DFO significantly alleviated the changes in BV/TV and Tb. Pf. Serum ELISA revealed no significant changes in ALT, AST, and Urea levels following treatment with FeDx, DFO, or NAR (Figs. 1H–1J). In addition, H&E staining of the liver showed clear and visible structures of liver lobules, polygonal liver cells with clear cell boundaries, and circular nuclei located at the center of the cells, displaying normal morphological features. H&E staining of the kidneys shows that the glomeruli and tubules in the cortical region are tightly interwoven, while the tubules in the medullary region are arranged neatly. Overall, the morphological features of liver and kidney tissues in each group were consistent with normal physiological characteristics, and no obvious histological abnormalities were observed, indicating that NAR at this dose did not cause significant pathological damage to liver and kidney tissues (Supplementary Fig. S1). These phenomena indicate that NAR has anti osteoporosis effects on iron overloaded mice, and the dosage is safe.

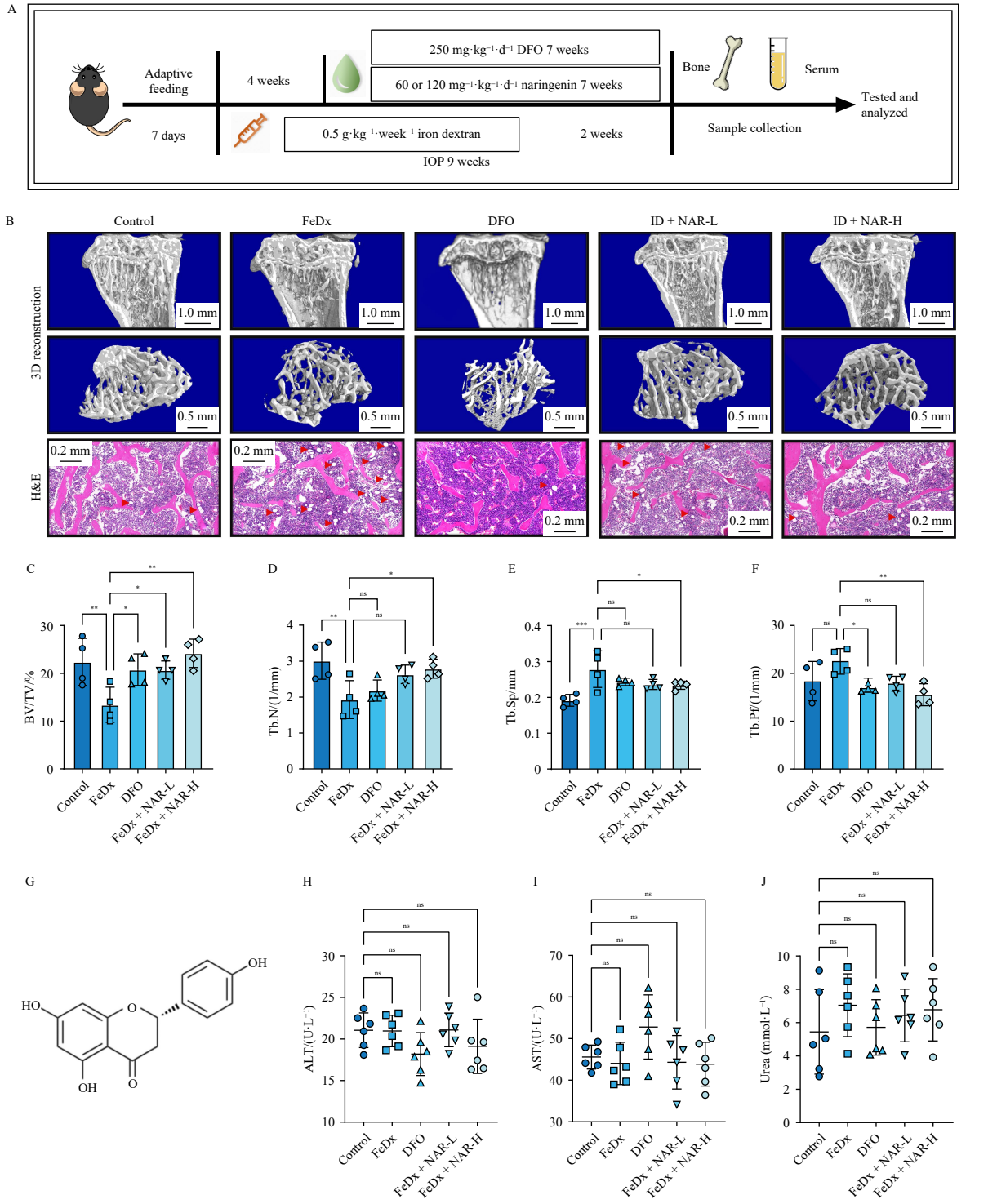


Fig. 1 NAR attenuates iron overload-associated bone microstructural changes. (A) Modeling method and flow chart of NAR treatment in iron overloaded animals. (B) 3D model of μCT scan reconstruction and H&E staining of mouse lower limb bone. The 3D model is shown in coronal and cross-sectional views, where the cross-sectional view shows the model after the removal of cortical bone. Pink in the H&E section is bone tissue, purple is medullary cavity cells, and round or oval blanks are fat vacuoles. Red arrows mark areas of fat vacuole concentration t (n = 4/group). (C–F) Bone microstructural parameters analysed for BV/TV, Tb. N, Tb. Sp, and Tb. Pf (n = 4/group). (G) Chemical structure of NAR . (H–J) ELISA assays for AST, ALT, and Urea (n = 6/group). All data are presented as mean ± SD. ns, $P > 0.05$; $^{*}P < 0.05$, $^{**}P < 0.01$, $^{***}P < 0.001$ *vs* Control; $^{\#}P < 0.05$ *vs* FeDx.

3.2. NAR attenuates the impairment of iron overload on the activity and apoptosis of MC3T3-E1 cells

To establish an iron-overloaded MC3T3-E1 cell model, FAC was used to elevate Fe^{3+} levels in culture media, as previously demonstrated in studies simulating iron overload environments. Notably, reported FAC concentrations varied substantially across prior work [22, 46, 47]. Thus, we empirically determined the optimal FAC concentration by assessing cell viability to balance iron supplementation with cellular tolerance.

CCK-8 assay results showed that low-concentration FAC (50 μmol·L^{-1}) slightly enhanced the viability of MC3T3-E1 cells at 24 and 48 h post-intervention, but this effect was reversed at 72 h (Fig. 2A). When the FAC concentration reached 200 μmol·L^{-1}, cell viability decreased significantly at 24, 48, and 72 h. The decline was more dramatic at 400 μmol·L^{-1}. Combining these findings with previous literature reports [22, 46, 47], we selected 400 μmol·L^{-1} as the optimal concentration for the iron-overload cell model, as

it induced the most pronounced decrease in cell viability.

The CCK8 results from NAR indicated that there was no inhibition of cellular activity in MC3T3-E1 cells at concentrations of 1–10 μmol·L^{-1} for 24, 48, and 72 h of intervention (Fig. 2B). In the presence of 400 μmol·L^{-1} FAC, cells treated with 1–10 μmol·L^{-1} of NAR were found to have elevated cell viability at both 5 and 10 μmol·L^{-1} at 48 and 72 h of intervention (Fig. 2C), so we chose 5 and 10 μmol·L^{-1} that had no inhibition of activity in normal cells but were protective of activity in iron overloaded cells for the subsequent study.

We also examined the expression of *Runx2*, an osteogenic trait gene, and *Col1a1*, a functional gene. The results showed that FAC at 400 μmol·L^{-1} inhibited the expression of *Runx2* and *Col1a1* and that the inhibition of *Runx2* was more pronounced, while NAR reversed this trend in a dose-related manner (Figs. 2D–2F). In the ALP activity assay and ARS staining, iron overload affected ALP activity and reduced the number of mineralised nodules. The FAC group showed significantly lighter staining compared to the Control group. Interestingly, NAR reduced the effect of iron overload on ALP activity and mineralisation capacity, and 10 μmol·L^{-1} had a better effect than 5 μmol·L^{-1} concentration on the recovery of ALP activity (Figs. 2G–2I).

3.3. NAR inhibits iron overload-associated ROS and LPO in MC3T3-E1 cells

DCFH-DA was used to indicate intracellular levels of ROS [48]. Fluorescence photographs showed a significant increase in the number of positive cells labelled by DCFH after intervention with FAC compared to the Control group, indicating an increased level of ROS in the cells. This was reversed after the NAR intervention (Figs. 3A and 3B).

Excess ROS can lead to cellular damage, and a decrease in MMP predicts damage to mitochondria [49], which we speculate may be associated with mitochondrial mtROS. MitoSOX red mitochondrial superoxide indicator was used to target the amount of mtROS specifically. The results showed that, compared to the Control group, there were more red fluorescent marked cells in iron overloaded MC3T3-E1 cells. At the same time, 5 and 10 μmol·L^{-1} NAR reversed this trend (Fig. 3C). Fluorescence quantification showed that the mean fluorescence intensity of cells was lower than the FAC group following NAR intervention, with a more significant decrease in the 10 μmol·L^{-1} NAR group than in the 5 μmol·L^{-1} NAR group (Fig. 3D).

On flow cytometric results BODIPY® C11 [50], MC3T3-E1 cells

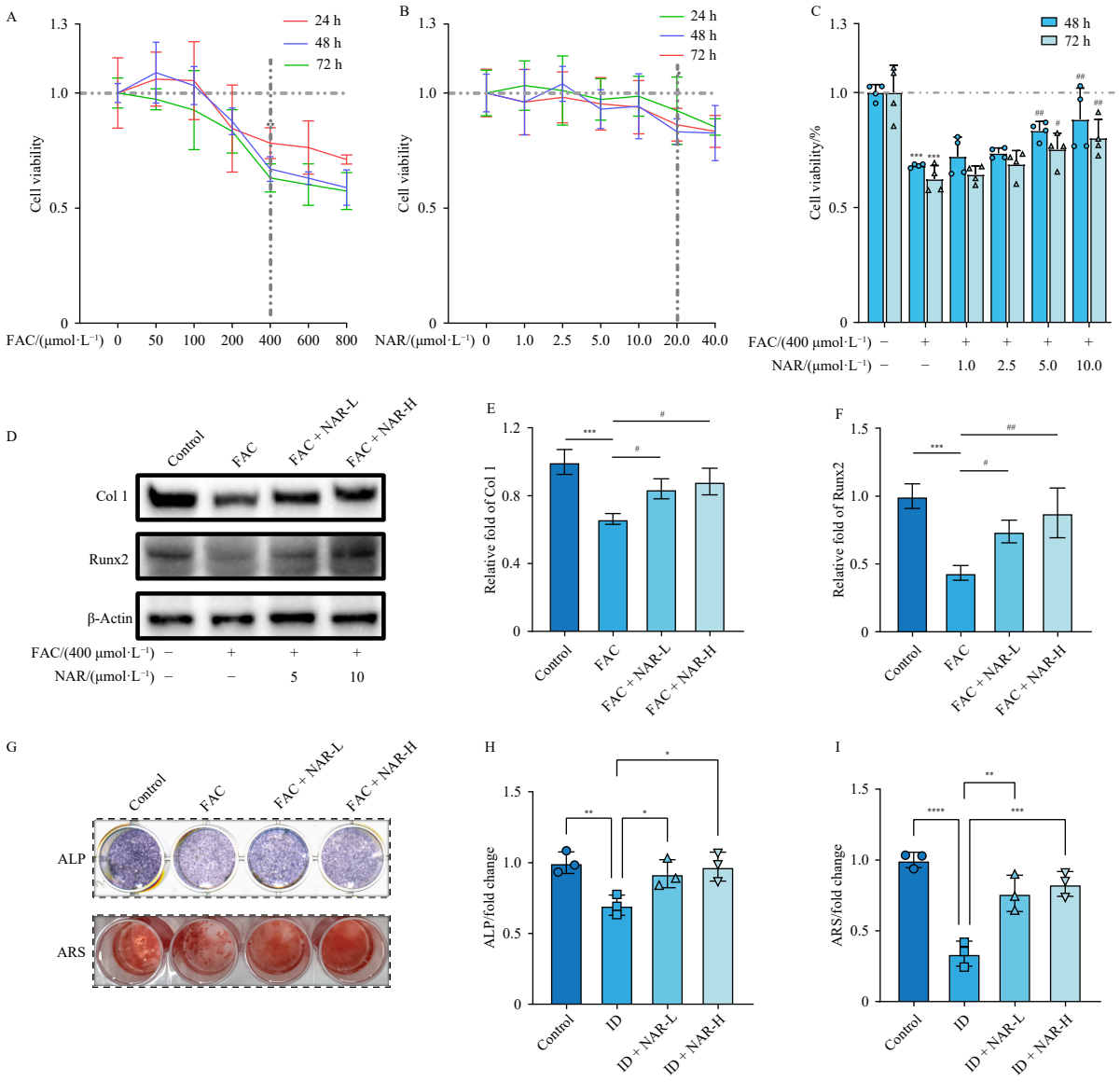


Fig. 2 NAR attenuates the effect of iron overload on MC3T3-E1 cells. (A) FAC affects cell viability in the CCK8 line graph ($^{**}P < 0.01$ *vs* FAC 0 μmol·L^{-1}). (B) NAR affects cell viability in the CCK8 line graph ($^{*}P < 0.05$ *vs* NAR 0 μmol·L^{-1}). (C) NAR action concentration screening CCK8 line graph ($^{***}P < 0.001$ *vs* FAC 0 μmol·L^{-1} + NAR 0 μmol·L^{-1}; $^{\#}P < 0.05$, $^{\#\#}P < 0.01$ *vs* FAC 400 μmol·L^{-1} + NAR 0 μmol·L^{-1}). (D) Western blot results for Col1a1, Runx2, and β-actin. (E) Quantitative results for Col-I. (F) Quantitative results for Runx2 protein. (G–I) BCIP/NBT alkaline phosphatase color development results and ARS mineralised nodule staining results. All data are presented as mean ± SD (A–C, n = 4/group; D–I, n = 3/group). $^{*}P < 0.05$, $^{**}P < 0.01$, $^{***}P < 0.001$, $^{****}P < 0.0001$.

under iron overload were overall more biased to the right of the diagonal, suggesting that the total percentage of emitted light at about 510 nm was higher than in the Control group under the same excitation conditions. After NAR treatment, the cells were generally shifted to the left, with an increased percentage of emitted light at about 590 nm and a decreased percentage at about 510 nm. The data from multiple experiments confirmed that the trend was statistically significant (Fig. 3E). The flow cytometric results reflected the same trend. It was more visually observed that a 10 μmol·L^{-1} concentration of NAR achieved a better reduction of ROS than a 5 μmol·L^{-1} concentration (Figs. 3F–3G). Total MDA was measured by colourimetric assay using an enzyme marker, and the results reflected the same direction (Fig. 3H), with NAR inhibiting iron overload-associated ROS and LPO in MC3T3-E1 cells.

3.4. NAR attenuates iron overload-associated mitochondrial dysfunction and affects autophagy

A decrease in MMP is one of the critical causes of apoptosis, and ROS can induce changes in MMP [51]. Under normal conditions, JC-1 probes accumulate in mitochondria as polymers and emit red fluorescence, whereas when FAC intervened, mitochondrial ΔΨm decreased, and some JC-1 probes could only exist as monomers and emit green fluorescence under fluorescence microscopy. In the flow cytometry assay, the trend in membrane potential was essentially the same, with results from multiple experiments suggesting that the changes were statistically significant (Figs. 4A and 4B). Surprisingly, the NAR intervention reduced the decrease in mitochondrial ΔΨm and the less green light was observed under fluorescence microscopy. In contrast, red light increased (Fig. 4C).

Previous studies have shown that iron overload can cause apoptosis in MC3T3-E1 cells [46]. Our flow cytometry results suggested that 400 μmol·L^{-1} FAC significantly increased the early and late apoptosis rate in MC3T3-E1 cells. Excitingly, NAR reduced the increase in apoptosis rate due to FAC, and a 10 μmol·L^{-1} concentration of NAR was somewhat better than 5 μmol·L^{-1} in reducing the late apoptosis rate (Figs. 4D and 4E).

Changes in MMP not only induce apoptosis but also alter autophagy levels. To investigate autophagy's potential role in NAR's protective effect, we also measured p62 and LC3 levels by protein blotting assay. FAC intervention significantly increased the LC3II/I ratio while decreasing p62 levels (Figs. 4F–4H). Surprisingly, NAR intervention reversed p62 levels and reduced changes in the LC3II/I ratio, suggesting that NAR attenuates autophagy in the iron overload model.

To investigate the role of autophagy in IOOP, we employed the autophagy inhibitor Mdivi-1 at 10 μmol·L^{-1} to selectively suppress dynamin-related protein 1 (Drp1) [52], thereby blocking the autophagic pathway, and observed whether iron overload-induced cellular effects were mitigated. Unexpectedly, Mdivi-1 failed to alleviate iron-overload-mediated oxidative damage and apoptosis; instead, it significantly exacerbated iron-induced inhibition of Col1a1 and Runx2 expression (Figs. 5A–5C) and further increased ROS levels in MC3T3-E1 cells (Figs. 5D–5G).

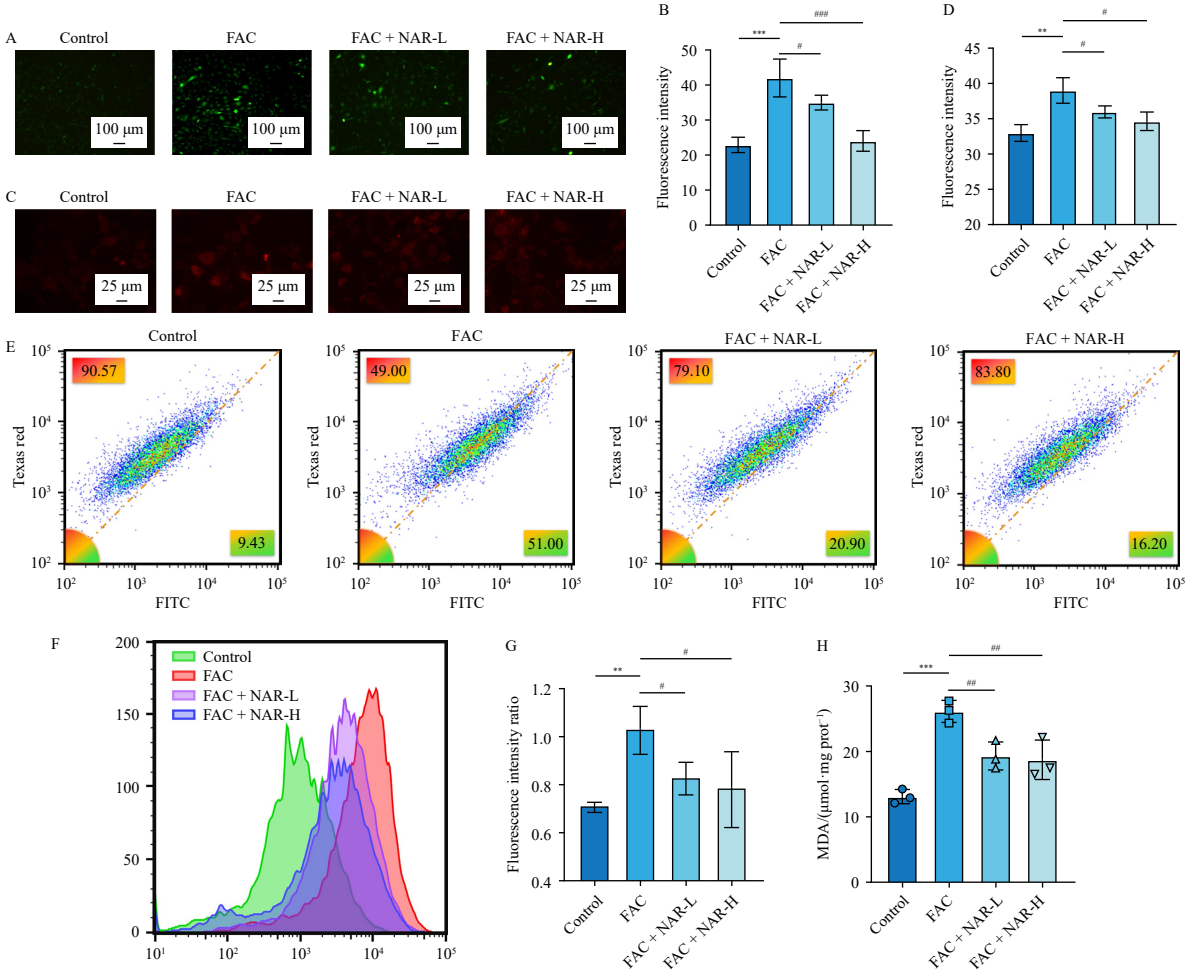


Fig. 3 NAR inhibits iron overload-associated ROS, mtROS and lipid peroxidation in MC3T3-E1 cells. (A) DCH-labelled intracellular ROS. (B) Quantification of fluorescence intensity of ROS content under fluorescence microscopy. (C) Fluorescence microscopy results of intracellular mtROS content. (D) Fluorescence quantification of intracellular mtROS content. (E) Flow cytometry results of relative intracellular LPO content. Numbers in each region represent the percentage of cells within the corresponding gate. (F and G) Ratio of DCF fluorescence signal accumulation detected by flow cytometry. (H) Quantitative results of MDA content assay. All data are presented as mean ± SD (n = 3). $^{*}P < 0.05$, $^{**}P < 0.01$, $^{***}P < 0.001$.

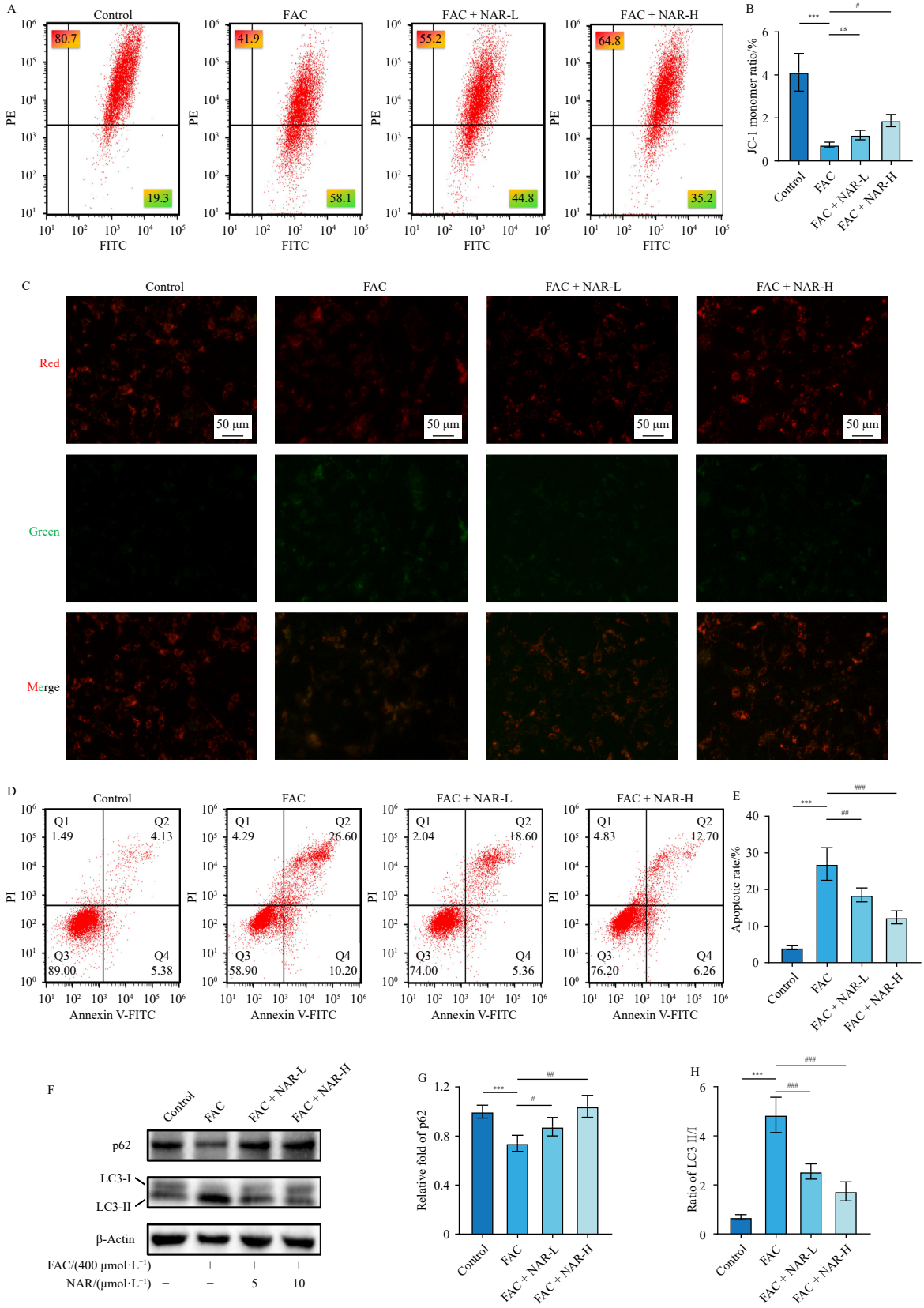


Fig. 4 NAR attenuates iron overload-associated decrease in MMP. (A) JC-1 flow cytometry results, the numbers indicate the percentage of cells above and below the horizontal line. (B) Quantitative analysis of JC-1 flow cytometry results, the vertical axis is the ratio of JC-1 monomer to JC-1 aggregates. (C) The results of JC-1 fluorescence microscopy show the most representative images. The red fluorescence mainly indicates JC-1 aggregates, and the green fluorescence mainly indicates JC-1 monomer. (D) Flow cytometry detection of apoptosis. Following the criteria reported in most literature, Q1 are physically damaged cells, Q2 are late apoptotic cells, Q3 are normal cells, and Q4 are early apoptotic cells. Numbers in the graph represent percentages. (E) Flow cytometry statistics for detection of apoptosis. (F) Western blot results for p62, LC3I/II, and β-actin. (G) Quantitative analysis of the grey scale values of the p62 bands. (H) Quantitative analysis of the grey scale values of the LC3I/II bands. All data are presented as mean ± SD (n = 3). $^{*}P < 0.05$, $^{**}P < 0.01$, $^{***}P < 0.001$.

However, Mdivi-1 treatment showed no statistically significant effects on mtROS production (Figs. 5H and 5I), apoptosis rates (Figs. 5J and 5K) , or JC-1 fluorescence-based MMP assessment (Figs. 5L and 5M) in iron-overloaded MC3T3-E1 cells. These findings indicate that autophagy inhibition is not an effective strategy to counteract iron-overload-induced decline in osteogenic capacity. Specifically, isolated inhibition of autophagy in iron-overloaded osteoblasts should be avoided, as it may exacerbate oxidative damage.

3.5. NAR-mediated amelioration of iron-overload-related osteogenic impairment is associated with Tfeb

To further screen the gene expression influenced by NAR in

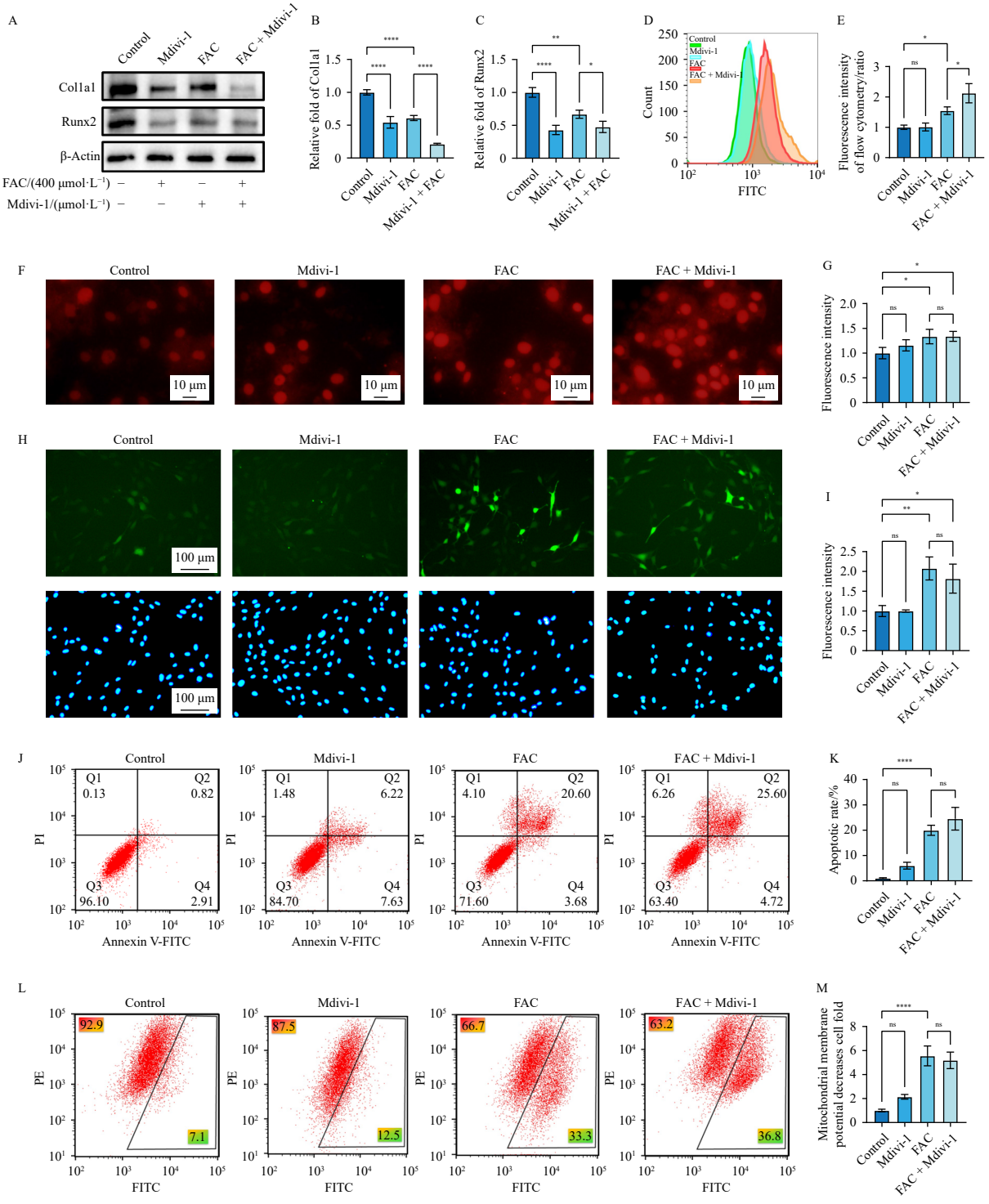


Fig. 5 Autophagy inhibition fails to rescue iron overload-induced osteoblast damage. (A) Western blot results for Col1a1, Runx2, and β-actin. (B) Quantitative results for Col-I. (C) Quantitative results for Runx2 protein. (D–E) Ratio of DCF fluorescence signal accumulation detected by flow cytometry. (F) DCH-labelled intracellular ROS. (G) Quantification of fluorescence intensity of ROS content under fluorescence microscopy. (H) Fluorescence microscopy results of intracellular mtROS content. (I) Fluorescence quantification of intracellular mtROS content. (J) Flow cytometry detection of apoptosis. Following the criteria reported in most literature, Q1 are physically damaged cells, Q2 are late apoptotic cells, Q3 are normal cells, and Q4 are early apoptotic cells. Numbers in the graph represent percentages. (K) Flow cytometry statistics for detection of apoptosis. (L) JC-1 flow cytometry results, the numbers indicate the percentage of cells above and below the horizontal line. Numbers in each region represent the percentage of cells within the corresponding gate. (M) Quantitative analysis of JC-1 flow cytometry results, the vertical axis is the ratio of JC-1 monomer to JC-1 aggregates. All data are presented as mean ± SD (n = 3/group). $^{*}P < 0.05$, $^{**}P < 0.01$, $^{***}P < 0.001$.

iron overload, we extracted the total RNA from the cancellous bone region of the lower femur in mice treated with FeDx and NAR-H, then conducted RNA-Seq detection. The gene expression abundance distribution of each sample demonstrated the robustness of sequencing reads across different samples (Supplementary Fig. S2A). Principal component analysis (PCA) revealed a distinct separation between the NAR and IR groups, highlighting notable differences in their global expression profiles (Supplementary Fig. S2B). Samples within the same group (IR1/IR2/IR3 or NAR1/NAR2/NAR3) showed high Pearson's correlation coefficients, indicating data reliability and reproducibility (Supplementary Fig. S2C). Using $|\log_2$ Fold change$| \geq 1$ and $P_{adj.} < 0.05$ as criteria, 115 DEGs were screened out after NAR intervention. Hierarchical clustering heatmaps grouped samples according to their treatment (IR or NAR), with distinct gene sets (C1−C4) exhibiting differential expression patterns, further emphasizing group specific expression characteristics (Supplementary Figs. S2D and S2E). Among these, 81 genes (e.g., *Col1a1*, *Col1a2*, *Acan*, *Serpina4a*) were up-regulated, while 34 genes (e.g., *Mmp12*, *Zfp967*, *Cstdc5*, *Gm14288*) were down-regulated, as presentedin the volcano plot (Supplementary Fig. S2F).

Gene Ontology (GO) analysis of DEGs revealed distinct functional patterns across biological processes, cellular components, and molecular functions. In the biological process (BP) category, significantly enriched terms included extracellular structure organization, extracellular matrix organization, bone development, and wound healing, indicating the predominant involvement of DEGs in tissue construction and repair-related biological pathways. Cellular component (CC) analysis demonstrated prominent enrichment in collagen-containing extracellular matrix, with additional associations observed in collagen trimer complexes and basement membrane structures. These findings collectively suggest preferential localization of DEG-encoded products within extracellular matrix architectures and related substructures. Molecular function (MF) characterization revealed three principal functional clusters: extracellular matrix structural constituents, collagen binding activity, and protease binding capacity. This functional profile underscores the dual roles of DEG products in mediating molecular interactions and maintaining structural integrity within extracellular environments (Supplementary Figs. S3A and S3B). Gene set enrichment analysis (GSEA) of GO terms identified significant entries ($P_{adj.} < 0.05$) that were subsequently ranked by normalized enrichment score (NES). The top six and bottom six most distinctive pathways were visualized in the GSEA enrichment plot (Supplementary Figs. S3C–S3H). Notably, the tripartite analytical outcomes consistently emphasize the critical involvement of DEGs in extracellular matrix remodeling and tissue homeostasis.

The KEGG pathway enrichment analysis results were visualized using bar plots, dot plots, and circular diagrams and the protein-protein interaction (PPI) network visualized the interaction network among DEGs, revealing that collagen formation-related genes (e.g., *Col1a1*, *Col1a2*) occupied central nodes (Supplementary Figs. S4A–S4D). Based on phenotypic results, our focus was on gene interaction relationships associated with iron overload and oxidative damage, which were located in the upper-left region of the PPI network. Tfeb was upregulated in NAR-treated bone tissues ($\log_2$ FC = 1.75, FDR = 0.0036), thereby identifying it as a potential regulatory target for NAR. The "ECM-receptor interaction" pathway demonstrating the most significant enrichment. Intriguingly, GSEA based on KEGG revealed a positive NES for the "ECM-receptor interaction−Mus musculus" pathway, whereas the "Lipid and atherosclerosis" pathway exhibited a negative NES following NAR intervention (Supplementary Figs. S4E and S4F). Examination of the "Lipid and atherosclerosis" gene set identified constituent genes associated with lipid peroxidation regulation (e.g., *Olr1*, *Sod2*) and cellular survival modulation (e.g., *Bcl2*, *Bax*), despite the absence of dedicated pathway entries for these processes in the KEGG repository.

Reactome database analysis (FDR < 0.05) highlighted the "Processing of capped intron-containing pre-mRNA" as the most prominently enriched pathway (Supplementary Figs. S4G and S4H). Notably, WikiPathway-based GSEA revealed significant enrichment in "Osteoclast signaling" and "Endochondral ossification" pathways (Supplementary Fig. S4I), suggesting the potential role of NAR in modulating bone homeostasis within the context of IOOP pathogenesis.

When co-administered with 50 μmol·L^{-1} eltrombopag (EO), a known Tfeb inhibitor, the ameliorative effects of NAR on Col1a1 and Runx2 downregulation were significantly attenuated (Figs. 6A–6D). Western blot analysis confirmed the upregulation of Tfeb protein following NAR intervention (Fig. 6E). The crystal structure of the human Tfeb bHLH-ZIP domain was retrieved from the Protein Data Bank (PDB) for molecular docking with NAR. Binding conformations exhibiting Vina scores < −5 kcal·mol^{-1} were systematically evaluated, with the top five poses visualized in 3D structural diagrams (Supplementary Fig. S5), suggesting potential multi-modal interactions between NAR and Tfeb. Notably, EO compromised NAR-mediated reductions in ROS/mtROS levels (Figs. 6F–6I) and abolished its protective effects against MMP depolarization (Figs. 6J–6M). These findings collectively demonstrate the functional dependency of NAR's biological efficacy on Tfeb activation.

3.6. NAR further modulates the Nrf2/Keap1 pathway via Tfeb

Previous studies have reported that Tfeb activates the Nrf2 antioxidant system [32, 53]. Western blotting results showed that Nrf2 levels increased in the FAC, FAC + NAR-L and FAC + NAR-H groups compared to the Control group (Figs. 7A–7F). Nrf2 and its inhibitor Keap1 are critical antioxidant regulatory systems. Immunofluorescence results showed that Nrf2 was activated in the cytoplasm and aggregated more towards the nucleus after FAC intervention. Interestingly, the activation of Nrf2 was facilitated by NAR intervention, with more Nrf2 entering the nucleus. At the same time, the cytoplasmic Keap1 was significantly reduced (Fig. 7G). Furthermore, the elevation of Nrf2 levels was more pronounced following NAR intervention, with the efficacy of NAR-H being superior to that of NAR-L. Notably, the phosphorylation level of Nrf2 at the Ser40 site was significantly increased in the NAR-H group. Heme oxygenase-1 (HO-1), a downstream factor of Nrf2, exhibited a consistent changing trend with Nrf2, whereas NAD(P)H quinone dehydrogenase 1 (Nqo1), another downstream target of Nrf2, was significantly upregulated exclusively following NAR administration. It is worth noting that no significant change in Keap1 expression was observed in the Control, FAC, and FAC + low-dose NAR (FAC + NAR-L) groups, while Keap1 was remarkably downregulated in the FAC + high-dose NAR (FAC + NAR-H) group.

To further validate Tfeb-mediated regulation of Nrf2, expression levels of Nrf2 and Keap1 were measured following EO treatment. Results showed that EO attenuated NAR-induced upregulation of Nrf2 but exerted no significant effect on Keap1 expression (Figs. 7H–7K). Notably, in FAC-treated cells, EO significantly downregulated Nrf2 and enhanced Keap1 expression.

3.7. Pharmacological and genetic inhibition of NRF2 attenuate the ROS scavenging effect of NAR

As iron overload correlates with intracellular peroxide accumulation, and as we found that NAR effectively enhanced the antioxidant capacity of cells *via* the Nrf2/Keap1 pathway, we used ML385, an inhibitor of Nrf2, for further studies. The results of the flow cytometric assay suggested that ML385 shifted MC3T3-E1

cells intervened by FAC and NAR together to the right and attenuated the ability of NAR to reduce LPO aggregation. At the same time, ML385 alone did not significantly increase LPO in normal cells. ML385 also attenuated the NAR-associated reduction in

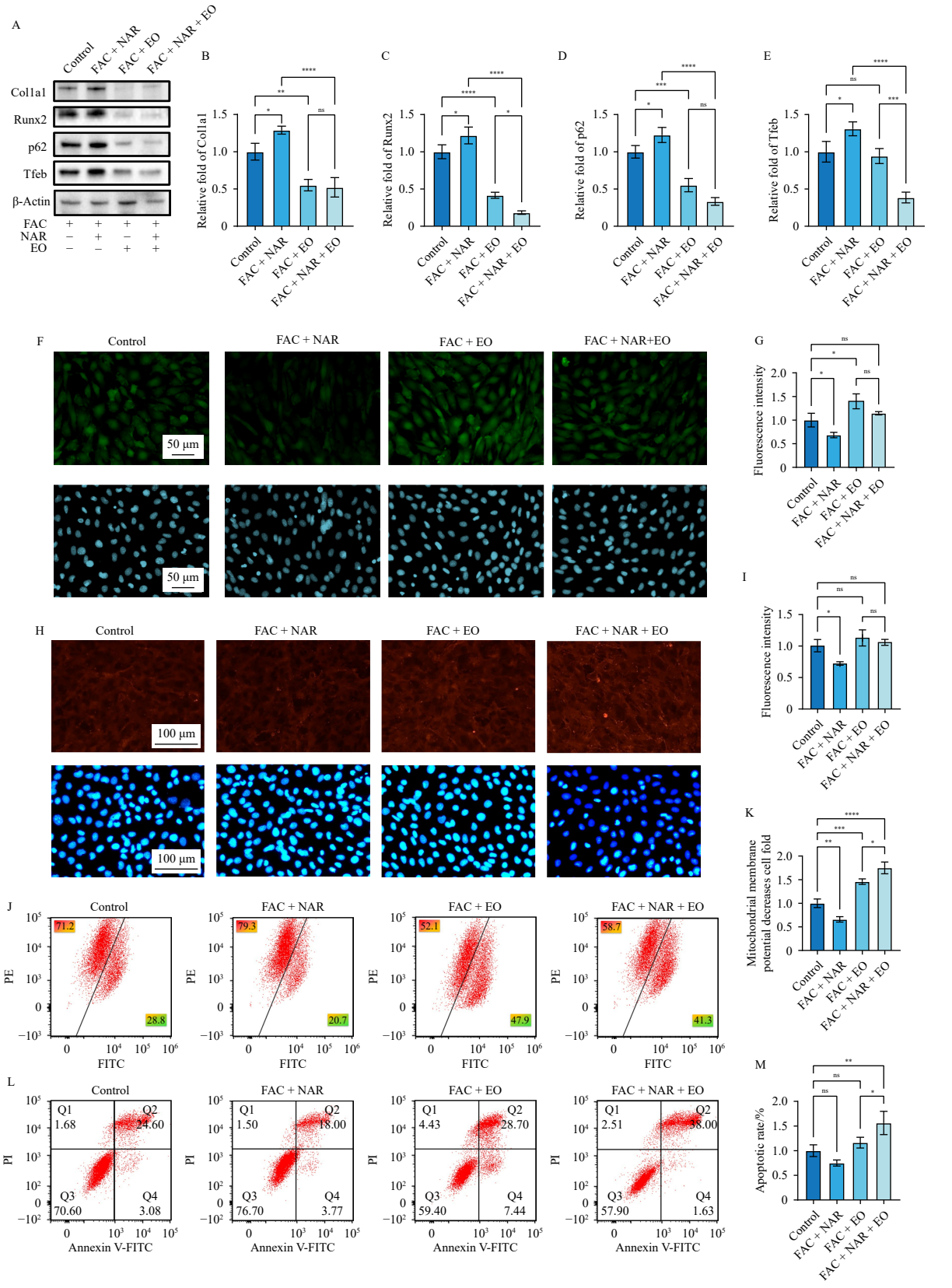


Fig. 6 NAR-mediated amelioration of iron-overload-related osteogenic impairment is associated with Tfeb. (A–E) Western blot results for Col1a1, Runx2, p62, Tfeb and β-actin and quantitative results. (F) DCH-labelled intracellular ROS. (G) Quantification of fluorescence intensity of ROS content under fluorescence microscopy. (H) Fluorescence microscopy results of intracellular mtROS content. (I) Fluorescence quantification of intracellular mtROS content. (J) JC-1 flow cytometry results, the numbers indicate the percentage of cells above and below the horizontal line. (K) Quantitative analysis of JC-1 flow cytometry results. (L) Flow cytometry detection of apoptosis. Following the criteria reported in most literature, Q1 are physically damaged cells, Q2 are late apoptotic cells, Q3 are normal cells, and Q4 are early apoptotic cells. Numbers in the graph represent percentages. (M) Flow cytometry statistics for detection of apoptosis. All data are presented as mean ± SD (n = 3). $^{*}P < 0.05$, $^{**}P < 0.01$, $^{***}P < 0.001$.

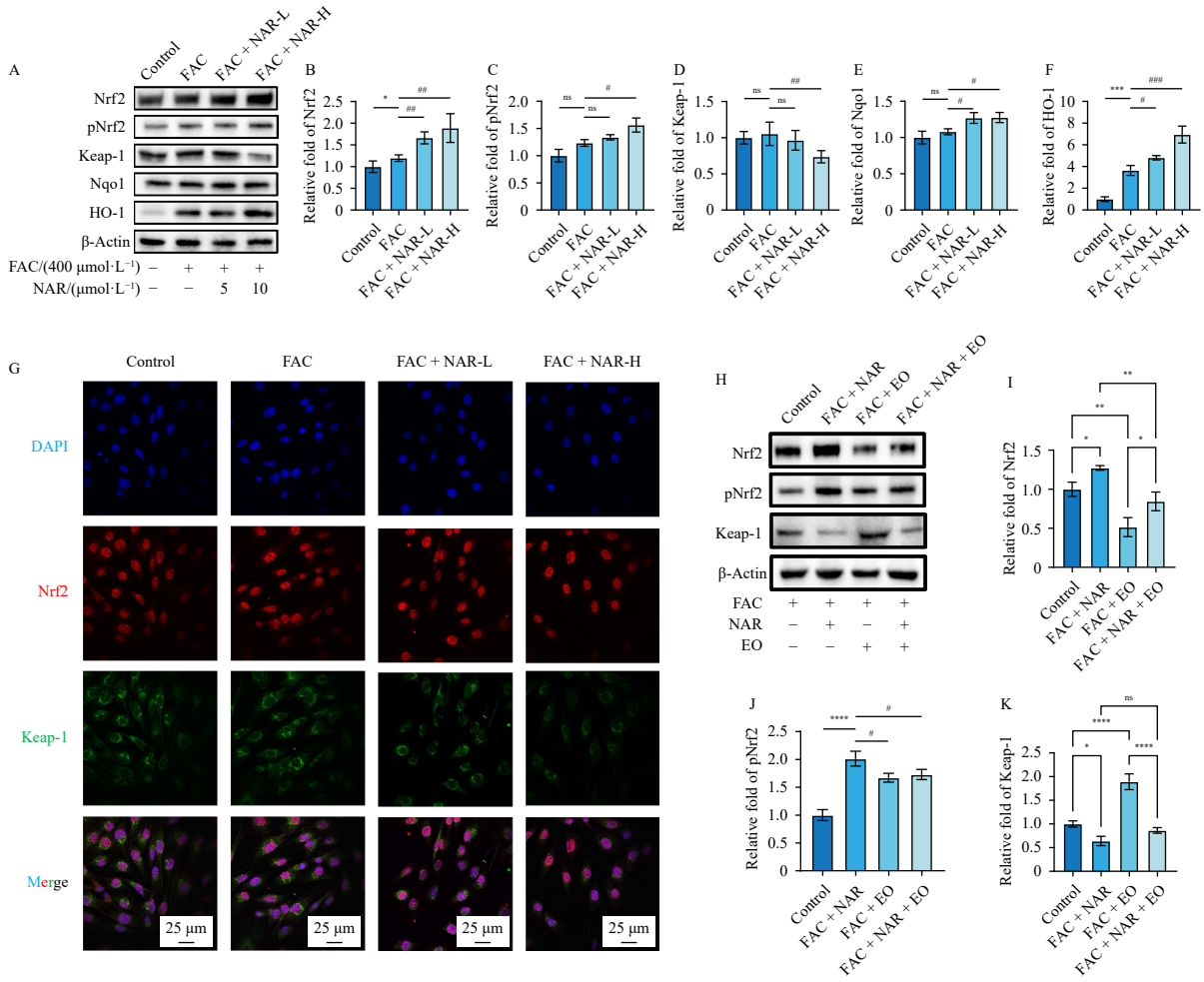


Fig. 7 NAR inhibits FAC-associated increase in mtROS by regulating the Nrf2/Keap1 pathway. (A) Western blot results for Nrf2, pNrf2, Keap1, Nqo1 and HO-1. (B–F) Quantitative analysis of the grey-scale values of Nrf2, pNrf2, Keap1, Nqo1 and HO-1 bands, respectively. (G) Immunofluorescence detection results of Nrf2, Keap1. Red fluorescence is Nrf2, green fluorescence is Keap1, and blue fluorescence is DAPI. (H–K) Western blot results for Nrf2, pNrf2, Keap1, β-actin and quantitative results. All data are presented as mean ± SD (n = 3). $^{*}P < 0.05$, $^{**}P < 0.01$, $^{***}P < 0.001$; $^{\#}P < 0.05$, $^{\#\#}P < 0.01$, $^{\#\#\#}P < 0.001$.

ROS. The use of ML385 substantially increased ROS levels compared to the FAC + NAR group, and the difference was statistically significant (Figs. 8A–8D).

In the Western blotting, ML385 reduced the expression of Nrf2 and its downstream factor, HO-1, while Keap1 showed no significant change after the intervention. For natural cells, ML385 similarly reduced the expression of Nrf2 and HO-1, but to a minor extent (Figs. 8E–8H). However, treatment with ML385 did not alter Tfeb expression (Figs. 8I and 8J), indicating that the regulation of Nrf2 by Tfeb is unidirectional.

To validate the findings from a genetic perspective, we employed small interfering RNA (siRNA) to knock down the expression of *Nfe2l2* (which encodes Nrf2) in MC3T3-E1 cells. The results demonstrated that knockdown of Nrf2 not only significantly increased the levels of mtROS, but also effectively reversed the restorative effect of NAR on ALP activity (Supplementary Fig. S6). Collectively, these findings indicate that the Nrf2 signaling pathway serves as a critical mediator for the cytoprotective actions of NAR.

Furthermore, to verify the necessity of Nrf2 in mediating the cytoprotective effects of NAR, flow cytometric analysis was performed after treatment with ML385, a specific Nrf2 inhibitor. The results demonstrated that NAR treatment significantly reduced the late apoptosis rate in iron-overloaded MC3T3-E1 cells. However, this protective effect of NAR was effectively reversed by co-treatment with ML385 (Figs. 9A and 9B).

It has been reported that p62 can regulate Keap1-Nrf2 interactions and induce downstream antioxidant effects by isolating Keap1 and can reduce Keap1 levels by inducing autophagic clearance of Keap1 [28, 54]. In the IP results, NAR treatment upregulated p62 levels compared to the FAC group. At the same time, p62-Keap1 binding became less after FAC intervention, whereas NAR intervention reversed this trend so that p62-Keap1 binding became tight after NAR intervention. This suggests that a greater proportion of Keap1 is bound and labelled by p62 in the cytoplasm (Figs. 9C–9E). Furthermore, analysis of Nrf2 content in the nucleus revealed that NAR intervention promoted nuclear translocation activation of Nrf2 (Fig. 9F). Immunohistochemical (IHC) analysis of bone tissues demonstrated that NAR treatment significantly upregulated the protein expression of both Tfeb and Nrf2 in cells located on the bone surface (Fig. 9G).

These results demonstrate that NAR enhances activation of the Nrf2 antioxidant system *via* Tfeb, thereby promoting formation of the p62-Keap1 complex to alleviate Keap1-mediated inhibition of Nrf2 and ultimately strengthening the osteogenic capacity of MC3T3-E1 cells under iron overload.

4. Discussion

OP is a metabolic disease of bone [55], and the study of the pathogenesis of OP has never stopped. Recently, studies have revealed the potential role of iron in OP [47]. As an essential element in the body, iron is extensively involved in many activities, including oxygen storage and transport, intracellular energy conversion, and nucleic acid metabolism [56]. There seems to be a consensus that appropriate intracellular iron levels are fundamental

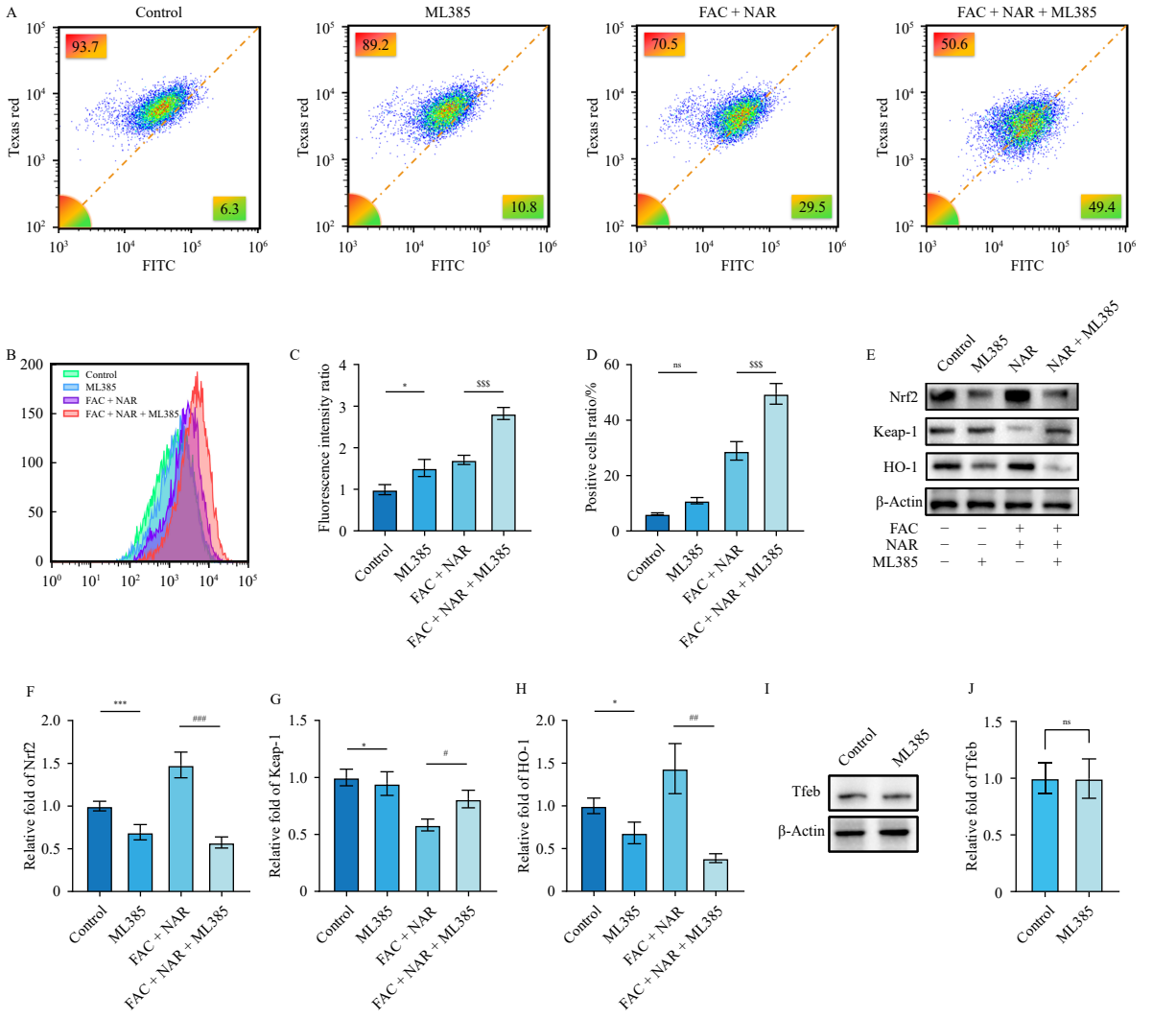


Fig. 8 ML385 substantially attenuates NAR-associated ROS and LPO scavenging. (A) Representative results of flow cytometry assay of intracellular LPO content. (B and C) Flow cytometry assay of ROS content and ratio analysis. (D) Statistics of the percentage of cells located in the lower right corner of the flow cytometry assay. (E–H) Western blot results and quantitative analysis of grey values for Nrf2, Keap1, and HO-1. (I and J) Western blot results for Tfeb. All data are presented as mean ± SD (n = 3). $^{*}P < 0.05$, $^{**}P < 0.01$, $^{***}P < 0.001$; $^{\#}P < 0.05$, $^{\#\#}P < 0.01$, $^{\#\#\#}P < 0.001$; $^{\$}P < 0.05$, $^{\$\$}P < 0.01$, $^{\$\$\$}P < 0.001$

to normal physiological function. Iron homeostasis depends on fine regulation but in pathological conditions, such as postmenopausal women, HH and other diseases [57]. In this study, incorporating previous reports and our experience, an iron overload model was constructed by intraperitoneal injection of iron dextran into C57BL/6J mice. The results showed a significant accumulation of iron in the blood of the mice. In addition to this, disruption of the physiomechanical structure of the trabeculae was seen in the micro-CT analysis of the upper tibia, and an increased number of fat vesicles in the medullary acavity and disruption of trabecular continuity was seen in sections of the lower femur. This pathological presentation has similarities to previous reports of what has been termed excess iron-associated bone loss [58]. However, it is undeniable that the induction of OP by iron overload is complex, and even studies carried out in typical HH patients have only uncovered part of the cause [59]. Therefore, unlike classical OP, the treatment of IOOP appears unclear. NAR-treated mice exhibited a significant improvement in trabecular bone microstructure and a reduction in fatty vesicles within the medullary cavity. Coincidentally, a recent study has reported a therapeutic effect of NAR on classical postmenopausal OP [60]. To distinguish these effects, we further investigated the role of NAR on an iron overload cell model.

When iron enters cells, it can generate large amounts of ROS in the Fenton or Haber-Weiss reaction [61], which can damage DNA and proteins [62] and is one of the critical signals in many cellular damages [63]. Because of this iron property, there is now a relatively large body of research linking iron overload-associated disease to ROS [64]. Accumulating studies have confirmed that ROS levels are significantly elevated in iron overload cell models. The accumulated ROS induced by iron overload attacks phospholipids in the cell membrane, leading to the accumulation of LPO and its metabolite MDA [65], which ultimately exacerbates cellular structural damage. In our study, we used FAC in MC3T3-E1 cells to simulate an iron overload environment while detecting intracellular oxide accumulation. The results showed that similar to previous iron overload studies, ROS levels were significantly increased within the iron overload cell model constructed by FAC [66]. Detection of cellular LPO content following FAC intervention using the BODIPY® C11 probe showed a significant increase in LPO levels in cells after iron overload treatment; concurrently, MDA content was also elevated post-induction, with LPO displaying a consistent trend with ROS. These results indicate that the iron overload model conforms to the characteristics of iron overload, ranging from the pathogenic factor to the main phenotypes. Although ferroptosis phenotypes may be associated with iron overload models—depending on iron concentration and cell type [67,68]—oxidative damage remains an extremely critical pathological feature of iron overload, regardless of the presence of ferroptosis. Surprisingly, in the NAR intervention experiment, the

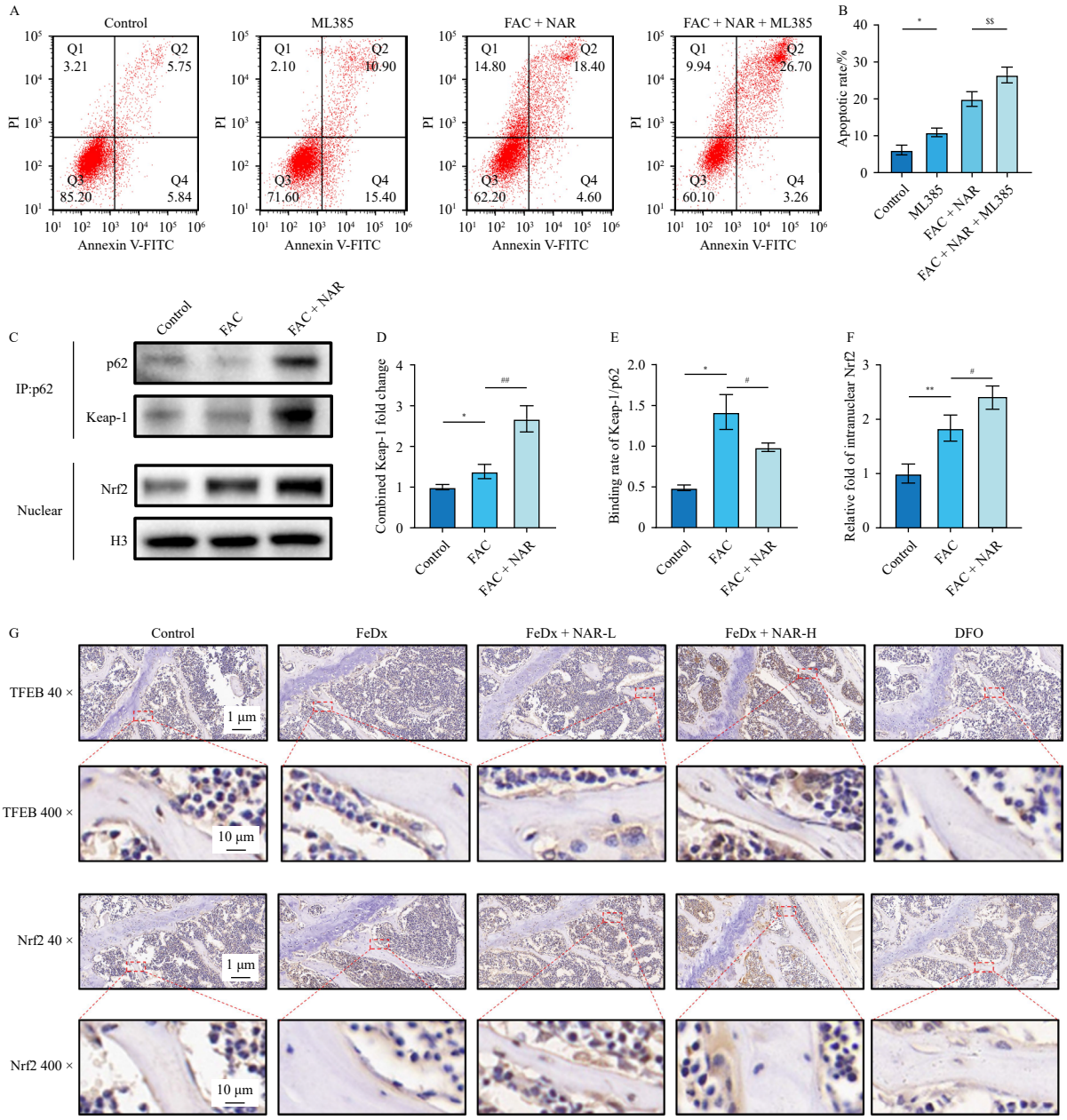


Fig. 9 NAR can control activation of the NRF-2/keap1 pathway through p62. (A) Results of apoptosis assay by flow cytometry. (B) Analysis of the percentage of late apoptotic cells. (C) IP results of p62, Keap1, Western blot analysis of nuclear Nrf2, histone H3, and intracytoplasmic Keap1 and β-actin. (D) The amount of p62 bound to Keap1 calculated from the grey scale values. (E and F) Binding rate of p62 to Keap1 and Nrf2 content in the nucleus, respectively. (G) IHC for Tfeb and Nrf2. All data are presented as mean ± SD ($n = 3$). $^{*}P < 0.05$, $^{**}P < 0.01$, $^{***}P < 0.001$; $^{\$}P < 0.05$, $^{\$\$}P < 0.01$, $^{\$\$\$}P < 0.001$.

abnormal accumulation of ROS, LPO, and MDA induced by iron overload was significantly inhibited. These findings indicate that NAR acts as a strong antioxidant in the iron overload model.

Previous studies have confirmed that iron overload is closely associated with cell apoptosis. A typical example is that in the characteristic iron overload state of HH, iron overload in glial cells can induce apoptosis [69]. The results of this study showed that iron overload significantly induced apoptosis in MC3T3-E1 cells, with the apoptosis level increasing by nearly 6-fold compared with normal cells. Meanwhile, NAR intervention could effectively inhibit the increase in apoptosis rate. The relationship between iron overload and apoptosis is relatively complex, but some studies have indicated that it is closely related to increased ROS [70], which can act as an intermediate mediator to damage cells and induce apoptosis. Notably, autophagy can protect cells from oxidative stress damage under iron overload [71]; therefore, it is necessary to explore whether autophagy and apoptosis undergo coordinated changes under iron overload [72]. Mitophagy is a key mechanism for clearing damaged mitochondria. As the central hub for cellular energy metabolism, mitochondria not only participate in the synthesis of iron-containing groups but also harbor the electron transport chain, which is the main source of ROS [73,74]. Therefore, similarly, ROS can serve as a bridge between cell apoptosis and autophagy. The results of this study showed that iron overload significantly decreased MMP, and MitoSOX red detection confirmed that iron overload induced a significant accumulation of mtROS, which was consistent with our speculation. At the same time, the LC3 II/I ratio increased while the p62 content decreased, indicating that intracellular autophagic flux was activated. Collectively, these findings support the conclusion that iron overload induces autophagy activation, which may resist ROS-induced damage and apoptosis.

Tfeb, a core member of the MITF-TFE family, is a basic helix-loop-helix leucine zipper (bHLH-Zip) transcription factor that participates in various physiological and pathological processes by regulating target gene expression [75]. The Nrf2/Keap1 signal-

ing pathway is a key regulatory system for cellular antioxidant capacity [76]. High-throughput screening results showed that NAR significantly upregulated Tfeb expression; combined with previous studies confirming that NAR can enhance Tfeb activity, this suggests that Tfeb may mediate the biological effects of NAR. Meanwhile, it was found that the expressions of Nrf2, HO-1 and Nqo1 were increased in MC3T3-E1 cells treated with FAC, while Keap1 expression showed no significant change. Notably, 10 μmol·L^{-1} NAR upregulated the expressions of Tfeb and Nrf2, while downregulating Keap1 expression. These results support the hypothesis that NAR activates the intracellular Tfeb/Nrf2 pathway and enhances cellular antioxidant capacity. This mechanism can explain the reduced levels of mtROS, ROS, LPO and MDA after NAR treatment. Notably, Tfeb can regulate the Nrf2/Keap1 signaling pathway [77]. Under physiological conditions, Keap1 forms a complex with Nrf2, retaining Nrf2 in the cytoplasm [78]; when induced by oxidative stress or antioxidants, the Nrf2/Keap1 complex dissociates, and Nrf2 translocates into the nucleus, binds to the ARE, and thereby promotes the transcription of antioxidant genes such as *HO-1*. However, the mechanism of this regulatory relationship in iron overload-related diseases remains unclear. To verify the regulatory relationship between Tfeb and Nrf2 under iron overload, we inhibited Tfeb and Nrf2 with EO and ML385, respectively. The results showed that inhibition of Nrf2 had no significant effect on Tfeb expression, while inhibition of Tfeb simultaneously regulated Nrf2 expression. This suggests that Tfeb can regulate Nrf2 rather than the reverse in the iron overload model of this study.

In addition, previous literature has shown that the Nrf2/Keap1 pathway itself is also involved in the regulation of the non-classical pathway mediated by p62 [79]. p62 can bind to Keap1 and induce its degradation [80]; therefore, NAR may exert a therapeutic effect on IOOP through p62 mediation, in a manner different from traditional iron overload therapies. To clarify whether the effect of NAR depends on p62, this study detected the binding rate of p62 to Keap1 and the expression level of Nrf2 in the nucleus after iron overload and NAR intervention. The results showed that while reducing mtROS and rescuing MMP collapse, NAR could also regulate cellular autophagy and upregulate p62 protein level. On the premise that there was no significant change in the total cellular Keap1 content, compared with the simple iron overload group, NAR intervention significantly increased the p62-Keap1 binding rate, and the Nrf2 level in the nucleus was synchronously upregulated. Given that Nrf2 activation can promote the clearance of mtROS and LPO, restore MMP and regulate autophagy, it is speculated that p62 may focus more on marking Keap1 in this process. As reported in previous studies, the Nrf2/Keap1/p62 axis can form a positive feedback loop to increase intracellular Nrf2 levels, and the Tfeb inhibitor EO can eliminate this effect, suggesting that this process is triggered by Tfeb [32, 53]. The above results support the following hypothesis: NAR enhances intracellular antioxidant capacity through this precise mechanism, thereby alleviating iron overload-related osteogenic dysfunction.

It is worth noting that although this study identified a potential new therapeutic drug NAR for IOOP and explored its novel mechanism of action, there are certain limitations in the experimental methods of this study. First, all studies and verifications were based on mouse models, and no validation has been conducted in human-derived cells or tissues. Second, the direct regulatory relationship between NAR and Nrf2 has not been further confirmed by Co-IP or surface plasmon resonance (SPR) technology. Finally, targeted pharmaceutical intervention methods such as MitoQ were not used to clarify the indispensability of mtROS in the process of NAR exerting its effects. These issues can be verified in further future studies, with the aim of further elucidating the pathogenesis of IOOP and exploring therapeutic approaches.

5. Conclusion

In summary, this study demonstrates that NAR ameliorates IOOP by activating the Tfeb/p62/Nrf2 pathway to enhance cellular antioxidant capacity, restore mitochondrial function, and protect osteoblastic cells from oxidative damage and apoptosis (Fig. 10). These findings provide a solid theoretical basis for the development of NAR as a therapeutic agent for IOOP and open new

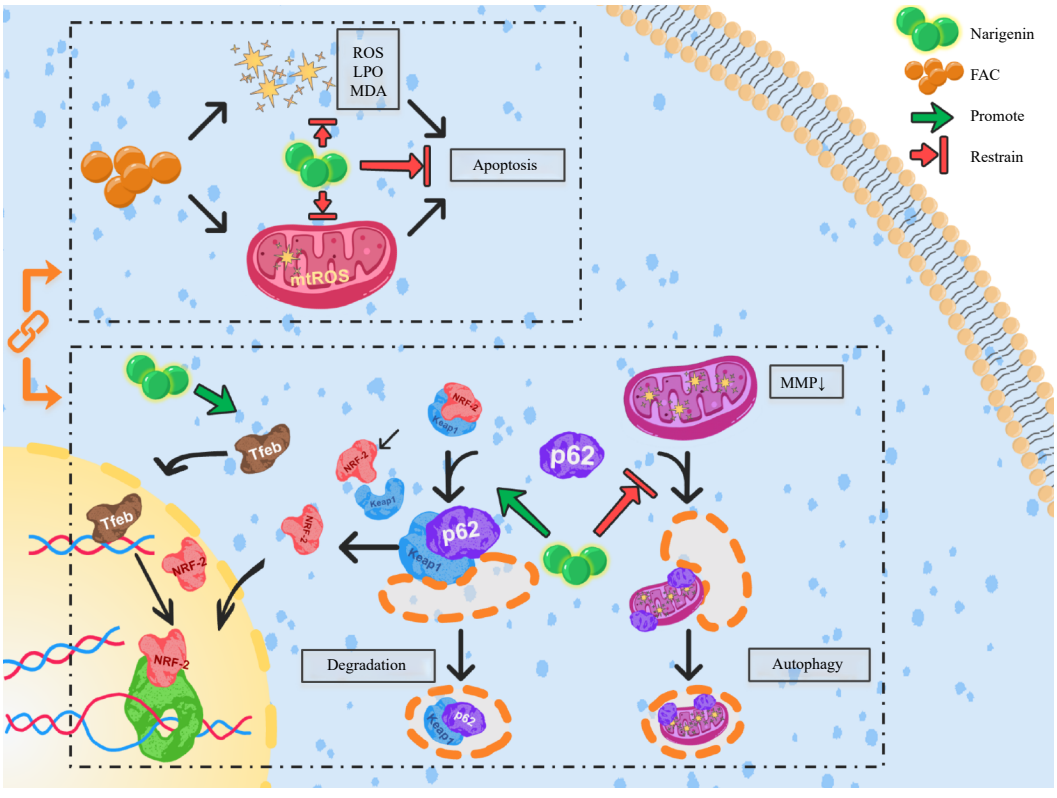


Fig. 10 Schematic representation of the role of NAR in modulating the Tfeb/p62/Nrf2/ pathway to mitigate iron overload damage.

avenues for the research of iron metabolism-related bone diseases.

Funding

This work was supported by the Guangzhou Municipal Science and Technology Program (No. 2023B03J0056), the Natural Science Foundation of Guangdong Province (Nos. 2024A1515012062 and 2021A1515010725), and the Scientific Research Project of Guangdong Provincial Bureau of Traditional Chinese Medicine (No. 20254028).

Supporting information

Supporting information for this work can be obtained by contacting the corresponding authors *via* E-mail.

Declaration of competing interest

These authors have no conflict of interest to declare.

References

1 Song SS, Guo YY, Yang YH, et al. Advances in pathogenesis and therapeutic strategies for osteoporosis. *Pharmacol Ther*. 2022;237:108168. https://doi.org/10.1016/j.pharmthera.2022.108168.
2 Yao Y, Cai XY, Chen Y, et al. Estrogen deficiency-mediated osteoimmunity in postmenopausal osteoporosis. *Med Res Rev*. 2025;45(2):561-575. https://doi.org/10.1002/med.22081.
3 Tao HQ, Li WM, Zhang W, et al. Urolithin A suppresses RANKL-induced osteoclastogenesis and postmenopausal osteoporosis by, suppresses inflammation and downstream NF-κB activated pyroptosis pathways. *Pharmacol Res*. 2021;174:105967. https://doi.org/10.1016/j.phrs.2021.105967.
4 Patel D, Wairkar S. Bone regeneration in osteoporosis: opportunities and challenges. *Drug Deliv Transl Res*. 2023;13(2):419-432. https://doi.org/10.1007/s13346-022-01222-6.
5 Wang LT, Chen LR, Chen KH. Hormone-related and drug-induced osteoporosis: a cellular and molecular overview. *Int J Mol Sci*. 2023;24(6):5814. https://doi.org/10.3390/ijms24065814.
6 Ensrud KE, Crandall CJ. Osteoporosis. *Ann Intern Med*. 2017;167(3):ITC17-ITC32. https://doi.org/10.7326/AITC201708010.
7 Li J, Chen X, Lu LY, et al. The relationship between bone marrow adipose tissue and bone metabolism in postmenopausal osteoporosis. *Cytokine Growth Factor Rev*. 2020;52:88-98. https://doi.org/10.1016/j.cytogfr.2020.02.003.
8 Cui YZ, Lv B, Li ZY, et al. Bone-targeted biomimetic nanogels re-establish osteoblast/osteoclast balance to treat postmenopausal osteoporosis. *Small*. 2024;20(6):e2303494. https://doi.org/10.1002/smll.202303494.
9 Liu X, An JJ. Dietary iron intake and its impact on osteopenia/osteoporosis. *BMC Endocr Disord*. 2023;23(1):154. https://doi.org/10.1186/s12902-023-01389-0.
10 Huang YR, Zhang J, Zhu YF, et al. BMP9 alleviates iron accumulation-induced osteoporosis *via* the USP10/FOXO1/GPX4 axis. *J Adv Res*. 2026;79:953-972. https://doi.org/10.1016/j.jare.2025.03.012.
11 Cai H, Zhang HM, He WT, et al. Iron accumulation and its impact on osteoporotic fractures in postmenopausal women. *J Zhejiang Univ Sci B*. 2023;24(4):301-311. https://doi.org/10.1631/jzus.B2200519.
12 Ru Q, Li YS, Xie WQ, et al. Fighting age-related orthopedic diseases: focusing on ferroptosis. *Bone Res*. 2023;11(1):12. https://doi.org/10.1038/s41413-023-00247-y.
13 Zhang H, Wang AF, Li GF, et al. Osteoporotic bone loss from excess iron accumulation is driven by NOX4-triggered ferroptosis in osteoblasts. *Free Radic Biol Med*. 2023;198:123-136. https://doi.org/10.1016/j.freeradbiomed.2023.01.026.
14 Ma JW, Wang AF, Zhang H, et al. Iron overload induced osteocytes apoptosis and led to bone loss in Hepcidin$^{-/-}$ mice through increasing sclerostin and RANKL/OPG. *Bone*. 2022;164:116511. https://doi.org/10.1016/j.bone.2022.116511.
15 Zhang C, Meng T, Dan Z, et al. Minocycline ameliorates osteoporosis induced by ovariectomy (OVX) and iron accumulation *via* iron chelation, bone metabolism regulation and inhibition of oxidative stress. *QJM*. 2020;116(11):969. https://doi.org/10.1093/qjmed/hcaa271.
16 Torti SV, Manz DH, Paul BT, et al. Iron and cancer. *Annu Rev Nutr*. 2018;38:97-125. https://doi.org/10.1146/annurev-nutr-082117-051732.
17 Guo Q, Qian C, Qian ZM. Iron metabolism and atherosclerosis. *Trends Endocrinol Metab*. 2023;34(7):404-413. https://doi.org/10.1016/j.tem.2023.04.003.
18 Jiang ZX, Qi GB, He XC, et al. Ferroptosis in osteocytes as a target for protection against postmenopausal osteoporosis. *Adv Sci (Weinh)*. 2024;11(12):e2307388. https://doi.org/10.1002/advs.202307388.
19 Zhu LW, You YC, Zhu MX, et al. Ferritin-Hijacking nanoparticles spatiotemporally directing endogenous ferroptosis for synergistic anticancer therapy. *Adv Mater*. 2022;34(51):e2207174. https://doi.org/10.1002/adma.202207174.
20 Stockwell BR. Ferroptosis turns 10: emerging mechanisms, physiological functions, and therapeutic applications. *Cell*. 2022;185(14):2401-2421. https://doi.org/10.1016/j.cell.2022.06.003.
21 Yun J, Rocic P, Pung YF, et al. Redox-dependent mechanisms in coronary collateral growth: the "redox window" hypothesis. *Antioxid Redox Signal*. 2009;11(8):1961-1974. https://doi.org/10.1089/ars.2009.2476.
22 Cen WJ, Feng Y, Li SS, et al. Iron overload induces G_1 phase arrest and autophagy in murine preosteoblast cells. *J Cell Physiol*. 2018;233(9):6779-6789. https://doi.org/10.1002/jcp.26405.
23 Jing XZ, Du T, Chen K, et al. Icariin protects against iron overload-induced bone loss *via* suppressing oxidative stress. *J Cell Physiol*. 2019;234(7):10123-10137. https://doi.org/10.1002/jcp.27678.
24 Yang F, Yang L, Li Y, et al. Melatonin protects bone marrow mesenchymal stem cells against iron overload-induced aberrant differentiation and senescence. *J Pineal Res*. 2017;63(3):12422. https://doi.org/10.1111/jpi.12422.
25 Luo C, Xu WJ, Tang X, et al. Canonical Wnt signaling works downstream of iron overload to prevent ferroptosis from damaging osteoblast differentiation. *Free Radic Biol Med*. 2022;188:337-350. https://doi.org/10.1016/j.freeradbiomed.2022.06.236.
26 Kapoor R, Sirohi VK, Gupta K, et al. Naringenin ameliorates progression of endometriosis by modulating Nrf2/Keap1/HO1 axis and inducing apoptosis in rats. *J Nutr Biochem*. 2019;70:215-226. https://doi.org/10.1016/j.jnutbio.2019.05.003.
27 Zhang DD. Thirty years of NRF2: advances and therapeutic challenges. *Nat Rev Drug Discov*. 2025;24(6):421-444. https://doi.org/10.1038/s41573-025-01145-0.
28 Zheng DC, Liu ZM, Zhou Y, et al. Urolithin B, a gut microbiota metabolite, protects against myocardial ischemia/reperfusion injury *via* p62/Keap1/Nrf2 signaling pathway. *Pharmacol Res*. 2020;153:104655. https://doi.org/10.1016/j.phrs.2020.104655.
29 Li YC, Xu B, Ren XY, et al. Inhibition of CISD2 promotes ferroptosis through ferritinophagy-mediated ferritin turnover and regulation of p62-Keap1-NRF2 pathway. *Cell Mol Biol Lett*. 2022;27(1):81. https://doi.org/10.1186/s11658-022-00383-z.
30 Ong AJS, Bladen CE, Tigani TA, et al. The KEAP1-NRF2 pathway regulates TFEB/TFE3-dependent lysosomal biogenesis. *Proc Natl Acad Sci U S A*. 2023;120(22):e2217425120. https://doi.org/10.1073/pnas.2217425120.
31 Chen L, Ning JL, Linghu L, et al. USP13 facilitates a ferroptosis-to-autophagy switch by activation of the NFE2L2/NRF2-SQSTM1/p62-KEAP1 axis dependent on the KRAS signaling pathway. *Autophagy*. 2025;21(3):565-582. https://doi.org/10.1080/15548627.2024.2410619.
32 Park JY, Kim S, Sohn HY, et al. TFEB activates Nrf2 by repressing its E3 ubiquitin ligase DCAF11 and promoting phosphorylation of p62. *Sci Rep*. 2019;9(1):14354. https://doi.org/10.1038/s41598-019-50877-8.
33 Butnariu M, Caunii A, Putnoky S. Reverse phase chromatographic behaviour of major components in *Capsicum annuum* extract. *Chem Cent J*. 2012;6(1):146. https://doi.org/10.1186/1752-153x-6-146.
34 Butnariu M. An analysis of *Sorghum halepense*'s behavior in presence of tropane alkaloids from *Datura stramonium* extracts. *Chem Cent J*. 2012;6(1):75. https://doi.org/10.1186/1752-153x-6-75.
35 Wang QY, Ou YJ, Hu GM, et al. Naringenin attenuates non-alcoholic fatty liver disease by down-regulating the NLRP3/NF-kappaB pathway in mice. *Br J Pharmacol*. 2020;177(8):1806-1821. https://doi.org/10.1111/bph.14938.
36 Butnariu M, Quispe C, Herrera-Bravo J, et al. The effects of thymoquinone on pancreatic cancer: evidence from preclinical studies. *Biomed Pharmacother*. 2022;153:113364. https://doi.org/10.1016/j.biopha.2022.113364.
37 Tutunchi H, Naeini F, Ostadrahimi A, et al. Naringenin, a flavanone with antiviral and anti-inflammatory effects: a promising treatment strategy against COVID-19. *Phytother Res*. 2020;34(12):3137-3147. https://doi.org/10.1002/ptr.6781.
38 Hua YQ, Zeng Y, Xu J, et al. Naringenin alleviates nonalcoholic steatohepatitis in middle-aged Apoe$^{(-/-)}$ mice: role of SIRT1. *Phytomedicine*. 2021;81:153412. https://doi.org/10.1016/j.phymed.2020.153412.
39 Zaragoza C, Villaescusa L, Monserrat J, et al. Potential therapeutic anti-inflammatory and immunomodulatory effects of dihydroflavones, flavones, and flavonols. *Molecules*. 2020;25(4):1017. https://doi.org/10.3390/molecules25041017.
40 Motallebi M, Bhia M, Rajani HF, et al. Naringenin: a potential flavonoid phytochemical for cancer therapy. *Life Sci*. 2022;305:120752. https://doi.org/10.1016/j.lfs.2022.120752.
41 Cao SY, Wang Y, Zhang YL, et al. Naringenin can inhibit the pyroptosis of osteoblasts by activating the Nrf2/HO-1 signaling pathway and alleviate the differentiation disorder of osteoblasts caused by microgravity. *J Agric Food Chem*. 2024;72(46):25586-25600. https://doi.org/10.1021/acs.jafc.4c05370.
42 Jin H, Jiang NN, Xu WS, et al. Effect of flavonoids from Rhizoma Drynariae on osteoporosis rats and osteocytes. *Biomed Pharmacother*. 2022;153:113379. https://doi.org/10.1016/j.biopha.2022.113379.
43 Li PY, Zhang S, Song H, et al. Naringin promotes skeletal muscle fiber remodeling by the AdipoR1-APPL1-AMPK signaling pathway. *J Agric Food Chem*. 2021;69(40):11890-11899. https://doi.org/10.1021/acs.jafc.1c04481.
44 Zhang GD, Li XF, Wu L, et al. Piezo1 channel activation in response to mechanobiological acoustic radiation force in osteoblastic cells. *Bone Res*. 2021;9(1):16. https://doi.org/10.1038/s41413-020-00124-y.
45 Wu GJ, Chen KY, Yang JD, et al. Naringin improves osteoblast mineralization and bone healing and strength through regulating estrogen receptor alpha-dependent alkaline phosphatase gene expression. *J Agric Food Chem*. 2021;69(44):13020-13033. https://doi.org/10.1021/acs.jafc.1c04353.
46 Wang F, Weng ZB, Song HZ, et al. Ferric ammonium citrate (FAC)-induced inhibition of osteoblast proliferation/differentiation and its reversal by

soybean-derived peptides (SDP). *Food Chem Toxicol.* 2021;156:112527. https://doi.org/10.1016/j.fct.2021.112527.
47 Che JM, Lv HH, Yang JC, et al. Iron overload induces apoptosis of osteoblast cells *via* eliciting ER stress-mediated mitochondrial dysfunction and p-eIF2alpha/ATF4/CHOP pathway *in vitro*. *Cell Signal.* 2021;84:110024. https://doi.org/10.1016/j.cellsig.2021.110024.
48 Huang CK, Gan DK, Luo FY, et al. Interaction mechanisms between the NOX4 /ROS and RhoA/ROCK1 signaling pathways as new anti- fibrosis targets of ursolic acid in hepatic stellate cells. *Front Pharmacol*. 2019;10:431. https://doi.org/10.3389/fphar.2019.00431.
49 Bock FJ, Tait SWG. Mitochondria as multifaceted regulators of cell death. *Nat Rev Mol Cell Biol.* 2020;21(2):85-100. https://doi.org/10.1038/s41580-019-0173-8.
50 Drummen GP, van Liebergen LC, Op den Kamp JA, et al. C11-BODIPY(581/591), an oxidation-sensitive fluorescent lipid peroxidation probe: (micro) spectroscopic characterization and validation of methodology. *Free Radic Biol Med.* 2002;33(4):473-490. https://doi.org/10.1016/s0891-5849(02)00848-1.
51 Sinha K, Das J, Pal PB, et al. Oxidative stress: the mitochondria-dependent and mitochondria-independent pathways of apoptosis. *Arch Toxicol.* 2013;87(7):1157-1180. https://doi.org/10.1007/s00204-013-1034-4.
52 Xian YS, Liu B, Shen T, et al. Enhanced SIRT3 expression restores mitochondrial quality control mechanism to reverse osteogenic impairment in type 2 diabetes mellitus. *Bone Res.* 2025;13(1):30. https://doi.org/10.1038/s41413-024-00399-5.
53 Sun XJ, Xiao SJ, Ma WQ, et al. Activation of TFEB protects against diabetic vascular calcification by improving autophagic flux and activating Nrf2 antioxidant system. *Am J Physiol Endocrinol Metab*. 2025;328(6):E924-E939. https://doi.org/10.1152/ajpendo.00161.2023.
54 Tan CT, Chang HC, Zhou QL, et al. MOAP-1-mediated dissociation of p62/SQSTM1 bodies releases Keap1 and suppresses Nrf2 signaling. *EMBO Rep.* 2021;22(1):e50854. https://doi.org/10.15252/embr.202050854.
55 Polyzos SA, Anastasilakis AD, Efstathiadou ZA, et al. Postmenopausal osteoporosis coexisting with other metabolic diseases: treatment considerations. *Maturitas.* 2021;147:19-25. https://doi.org/10.1016/j.maturitas.2021.02.007.
56 Zhang XB, Liang YS, Zhang FY, et al. Osteoporosis: molecular pathogenesis and therapeutic interventions. *Mol Biomed.* 2025;6(1):98. https://doi.org/10.1186/s43556-025-00349-5.
57 Wang D, Shen JH, Wang Y, et al. Mechanisms of ferroptosis in bone disease: a new target for osteoporosis treatment. *Cell Signal*. 2025;127:111598. https://doi.org/10.1016/j.cellsig.2025.111598.
58 Zhang QL, Zhao L, Shen Y, et al. Curculigoside protects against excess-iron-induced bone loss by attenuating Akt-FoxO1-dependent oxidative damage to mice and osteoblastic MC3T3-E1 cells. *Oxid Med Cell Longev*. 2019;2019:9281481. https://doi.org/10.1155/2019/9281481.
59 Baschant U, Altamura S, Steele-Perkins P, et al. Iron effects versus metabolic alterations in hereditary hemochromatosis driven bone loss. *Trends Endocrinol Metab.* 2022;33(9):652-663. https://doi.org/10.1016/j.tem.2022.06.004.
60 Gera S, Sampathi S, Maddukuri S, et al. Therapeutic potential of naringenin nanosuspension: *in vitro* and *in vivo* anti-osteoporotic studies. *Pharmaceutics*. 2022;14(7):1449. https://doi.org/10.3390/pharmaceutics14071449.
61 Cui ZC, Gu GH, Chen F, et al. Targeting Irgm1 to combat osteoporosis: suppressing ROS and restoring bone remodeling. *Cell Death Dis.* 2025;16(1):651. https://doi.org/10.1038/s41419-025-07965-7.
62 Ford SA, King KC. *In vivo* microbial coevolution favors host protection and plastic downregulation of immunity. *Mol Biol Evol*. 2021;38(4):1330-1338. https://doi.org/10.1093/molbev/msaa292.
63 Yang L, Wang H, Yang X, et al. Auranofin mitigates systemic iron overload and induces ferroptosis *via* distinct mechanisms. *Signal Transduct Target Ther*. 2020;5(1):138. https://doi.org/10.1038/s41392-020-00253-0.
64 Tian Q, Qin B, Gu YF, et al. ROS-mediated necroptosis is involved in iron overload-induced osteoblastic cell death. *Oxid Med Cell Longev*. 2020;2020:1295382. https://doi.org/10.1155/2020/1295382.
65 Zhao HJ, Zhang JJ, Liu XC, et al. The antioxidant activities of alkalic-extractable polysaccharides from *Coprinus comatus* on alcohol-induced liver injury in mice. *Sci Rep.* 2018;8(1):11695. https://doi.org/10.1038/s41598-018-30104-6.
66 Huan H, Lyamzaev KG, Panteleeva AA, et al. Mitochondrial lipid peroxidation is necessary but not sufficient for induction of ferroptosis. *Front Cell Dev Biol*. 2024;12:1452824. https://doi.org/10.3389/fcell.2024.1452824.
67 Zeng WJ, Wang FX, Cui ZK, et al. Inhibition of ferroptosis counteracts the advanced maternal age-induced oocyte deterioration. *Cell Death Differ*. 2025;32(6):1071-1085. https://doi.org/10.1038/s41418-025-01456-0.
68 Huan XJ, Li JG, Chu ZB, et al. Dysregulation of iron homeostasis mediated by FTH increases ferroptosis sensitivity in TP53-mutant glioblastoma. *Neurosci Bull*. 2025;41(4):569-582. https://doi.org/10.1007/s12264-024-01322-y.
69 Nobuta H, Yang N, Ng YH, et al. Oligodendrocyte death in Pelizaeus-Merzbacher disease is rescued by iron chelation. *Cell Stem Cell*. 2019;25(4):531-541.e6. https://doi.org/10.1016/j.stem.2019.09.003.
70 Camiolo G, Barbato A, Giallongo C, et al. Iron regulates myeloma cell/macrophage interaction and drives resistance to bortezomib. *Redox Biol.* 2020;36:101611. https://doi.org/10.1016/j.redox.2020.101611.
71 Xia F, Fu YY, Xie HZ, et al. Suppression of ATG4B by copper inhibits autophagy and involves in Mallory body formation. *Redox Biol.* 2022;52:102284. https://doi.org/10.1016/j.redox.2022.102284.
72 Hao L, Zhang AB, Lv DS, et al. EGCG activates Keap1/P62/Nrf2 pathway, inhibits iron deposition and apoptosis in rats with cerebral hemorrhage. *Sci Rep.* 2024;14(1):31474. https://doi.org/10.1038/s41598-024-82938-y.
73 Palma FR, Gantner BN, Sakiyama MJ, et al. ROS production by mitochondria: function or dysfunction? . *Oncogene*. 2024;43(5):295-303. https://doi.org/10.1038/s41388-023-02907-z.
74 DiGiovanni LF, Khroud PK, Carmichael RE, et al. ROS transfer at peroxisome-mitochondria contact regulates mitochondrial redox. *Science*. 2025;389(6756):157-162. https://doi.org/10.1126/science.adn2804.
75 Wu Y, Xun Y, Zhang JQ, et al. Resveratrol attenuates oxalate-induced renal oxidative injury and calcium oxalate crystal deposition by regulating TFEB-induced autophagy pathway. *Front Cell Dev Biol*. 2021;9:638759. https://doi.org/10.3389/fcell.2021.638759.
76 Zhang J, Zhang MZ, Tatar M, et al. Keap1-independent Nrf2 regulation: a novel therapeutic target for treating kidney disease. *Redox Biol.* 2025;82:103593. https://doi.org/10.1016/j.redox.2025.103593.
77 Sanchez-de-Diego C, Pedrazza L, Pimenta-Lopes C, et al. NRF2 function in osteocytes is required for bone homeostasis and drives osteocytic gene expression. *Redox Biol.* 2021;40:101845. https://doi.org/10.1016/j.redox.2020.101845.
78 Liberti D, Alfieri ML, Monti DM, et al. A melanin-related phenolic polymer with potent photoprotective and antioxidant activities for dermo-cosmetic applications. *Antioxidants (Basel)*. 2020;9(4):270. https://doi.org/10.3390/antiox9040270.
79 Kong L, Deng J, Zhou X, et al. Sitagliptin activates the p62-Keap1-Nrf2 signalling pathway to alleviate oxidative stress and excessive autophagy in severe acute pancreatitis-related acute lung injury. *Cell Death Dis.* 2021;12(10):928. https://doi.org/10.1038/s41419-021-04227-0.
80 Wang XX, Li M, Xu XW, et al. BNIP3-mediated mitophagy attenuates hypoxic-ischemic brain damage in neonatal rats by inhibiting ferroptosis through P62-KEAP1-NRF2 pathway activation to maintain iron and redox homeostasis. *Acta Pharmacol Sin.* 2025;46(1):33-51. https://doi.org/10.1038/s41401-024-01365-x.